

**Abstract**

**Measurement of total hadronic differential cross  
sections in the LArIAT experiment**

Elena Gramellini

2018

Abstract goes here. Limit 750 words.

# **Measurement of total hadronic differential cross sections in the LArIAT experiment**

A Dissertation  
Presented to the Faculty of the Graduate School  
of  
Yale University  
in Candidacy for the Degree of  
Doctor of Philosophy

by  
Elena Gramellini

Dissertation Director: Bonnie T. Fleming

Date you'll receive your degree

Copyright © 2017 by Elena Gramellini

All rights reserved.

# Contents

<b>Acknowledgements</b>	<b>v</b>
<b>0 Introduction</b>	<b>1</b>
<b>1 The theoretical framework</b>	<b>2</b>
1.1 The Standard Model . . . . .	2
1.2 Neutrinos: tiny cracks in the Standard Model . . . . .	4
1.2.1 Neutrinos in the Standard Model . . . . .	4
1.2.2 Neutrino Oscillations . . . . .	6
1.2.3 Make up of Neutrino Interactions . . . . .	7
1.3 Beyond the Standard Model . . . . .	11
1.3.1 Open Questions in Neutrino Physics . . . . .	11
1.3.2 Towards a more fundamental theory: GUTs . . . . .	15
1.4 Motivations for Hadronic Cross Sections in Argon . . . . .	18
1.4.1 Pion-Argon Total Hadronic Cross Section . . . . .	19
1.4.2 Kaon-Argon Total Hadronic Cross Section . . . . .	29
<b>2 Liquid Argon Detectors at the Intensity Frontier</b>	<b>34</b>
2.1 The Liquid Argon Time Projection Chamber Technology . . . . .	34
2.1.1 TPCs, Neutrinos & Argon . . . . .	34
2.1.2 LArTPC: Principles of Operation . . . . .	36

2.1.3	Liquid Argon: Ionization Charge . . . . .	39
2.1.4	Liquid Argon: Scintillation Light . . . . .	44
2.1.5	Signal Processing and Event Reconstruction . . . . .	48
2.2	The Intensity Frontier Program . . . . .	53
2.2.1	Prospects for LArTPCs in Neutrino Physics: SBN and DUNE	53
2.2.2	Prospects for LArTPCs in GUT Physics: DUNE . . . . .	54
2.2.3	Enabling the next generation of discoveries: LArIAT . . . . .	55

# Acknowledgements

A lot of people are awesome, especially you, since you probably agreed to read this when it was a draft.

# **Chapter 0**

## **Introduction**

# Chapter 1

## The theoretical framework

### 1.1 The Standard Model

The Standard Model (SM) of particle physics is the most accurate theoretical description of the subatomic world and, in general, one of the most precisely tested theories in the history of physics. The SM describes the strong, electromagnetic and weak interactions among elementary particles in the framework of quantum field theory, accounting for the unification of electromagnetic and weak interactions for energies above the vacuum expectation value (VEV) of the Higgs field. The SM does not describe gravity or general relativity.

The Standard Model is a gauge theory based on the local group of symmetry

$$G_{SM} = SU(3)_C \otimes SU(2)_T \otimes U(1)_Y \quad (1.1)$$

where the subscripts indicate the conserved charges: the strong charge, or color C, the weak isospin T (or rather its third component T<sub>3</sub>) and the hypercharge Y. These quantities can be related to the electric charge Q through the Gell-Mann-Nishijima relation:

$$Q = \frac{Y}{2} + T_3. \quad (1.2)$$

Generation	I	II	III	T	Y	Q
Leptons	$\begin{pmatrix} \nu_e \\ e \end{pmatrix}_L$	$\begin{pmatrix} \nu_\mu \\ \mu \end{pmatrix}_L$	$\begin{pmatrix} \nu_\tau \\ \tau \end{pmatrix}_L$	1/2 -1/2	-1 -1	0 -1
	$e_R$	$\mu_R$	$\tau_R$	0	-2	1
Quarks	$\begin{pmatrix} u \\ d' \end{pmatrix}_L$	$\begin{pmatrix} c \\ s' \end{pmatrix}_L$	$\begin{pmatrix} t \\ b' \end{pmatrix}_L$	1/2 -1/2	1/3 1/3	2/3 -1/3
	$u_R$ $d'_R$	$c_R$ $s'_R$	$t_R$ $b'_R$	0 0	4/3 -2/3	2/3 -1/3

Table 1.1: SM elementary fermions. The subscripts L and R indicate respectively the negative helicity (left-handed) and the positive helicity (right-handed).

In the quantum field framework, the elementary particles correspond to the irreducible representations of the  $G_{SM}$  symmetry group. In particular, the particles are divided in two categories, fermions and bosons, according to their spin-statistics. Described by the Fermi-Dirac statistics, fermions have half-integer spin and are sometimes called “matter-particles”. Bosons or “force carriers” have integer spin, follow the Bose-Einstein statistics and mediate the interaction between fermions. The fundamental fermions and their quantum numbers are listed in Tab 1.1.

Quarks can interact via all three the fundamental forces; they are triplets of  $SU(3)_C$ , that is they can exist in three different colors: C = R, G, B. If one chooses a base where  $u$ ,  $c$  and  $t$  quarks are simultaneously eigenstates of both the strong and the weak interactions, the remaining eigenstates are usually written as  $d$ ,  $s$  and  $b$  for the strong interaction and  $d'$ ,  $s'$  and  $b'$  for the weak interaction, because the latter ones are the result of a Cabibbo rotation on the first ones. Charged leptons interact via the weak and the electromagnetic forces, while neutrinos only interact via the weak force. The gauge group univocally determines the number of gauge bosons that carry the interaction; the gauge bosons correspond to the generators

of the group: eight gluons (g) for the strong interaction, one photon ( $\gamma$ ) and three bosons ( $W^\pm$ ,  $Z^0$ ) for the electroweak interaction. A gauge theory by itself can not provide a description of massive particles, but it is experimentally well known that most of the elementary particles have non-zero masses. The introduction of massive fields in the Standard Model lagrangian would make the theory non-renormalizable, and - so far - mathematically impossible to handle. This problem is solved in the SM by the introduction of a scalar iso-doublet  $\Phi(x)$ , the Higgs field, which gives mass to  $W^\pm$  and  $Z^0$  gauge bosons through the electroweak symmetry breaking mechanism and to the fermions through Yukawa coupling [59, 60]. The discovery of the Higgs boson in 2012 by the LHC experiments [31, 32] marked the ultimate confirmation of a long history of successful predictions by the SM.

## 1.2 Neutrinos: tiny cracks in the Standard Model

### 1.2.1 Neutrinos in the Standard Model

Neutrino were introduced in the SM as left-handed massless Weyl spinors. The Dirac equation of motion

$$(i\gamma^\mu \partial_\mu - m)\psi = 0 \quad (1.3)$$

for a fermionic field

$$\psi = \psi_L + \psi_R \quad (1.4)$$

is equivalent to the equaitons

$$i\gamma^\mu \partial_\mu \psi_L = m\psi_R \quad (1.5)$$

$$i\gamma^\mu \partial_\mu \psi_R = m\psi_L \quad (1.6)$$

for the chiral fields  $\psi_R$  and  $\psi_L$ , whose evolution in space and time is coupled through the mass  $m$ . If the fermion is massless, the chiral fields decouple and the

fermion can be described by a single Weyl spinor with two independent components [95]. Pauli initially rejected the description of a physical particle through a single Weyl spinor because of its implication of parity violation. In fact, since the spatial inversion operator throws  $\psi_R \leftrightarrow \psi_L$ , parity is conserved only if the both the chiral components exist at the same time. For the neutrino introduction in the SM, experiments came in help of the theoretical description. The constraint of parity conservation weakened after Wu's experiment in 1957 [98]. Additionally, there was no experimental indication for massive neutrinos, nor evidence of interaction via the neutrino right-handed component.

The symmetry group  $SU(2)_T \otimes U(1)_Y$  is the only group relevant for neutrino interactions. The SM electroweak lagrangian is the most general renormalizable lagrangian invariant under the local symmetry group  $SU(2)_T \otimes U(1)_Y$ . The lagrangian couples the weak isotopic spin doublets and singlets described in Table 1.1 with the gauge bosons  $A_a^\mu$  ( $a = 1, 2, 3$ ) and  $B^\mu$ , and Higgs doublet  $\Phi(x)$ :

$$\begin{aligned}
\mathcal{L} = & i \sum_{\alpha=e,\mu,\tau} \bar{L}'_{\alpha L} \not{D} L'_{\alpha L} + i \sum_{\alpha=1,2,3} \bar{Q}'_{\alpha L} \not{D} Q'_{\alpha L} \\
& + i \sum_{\alpha=e,\mu,\tau} \bar{l}'_{\alpha R} \not{D} l'_{\alpha R} + i \sum_{\alpha=d,s,b} \bar{q}'^D_{\alpha R} \not{D} q'^D_{\alpha R} + i \sum_{\alpha=u,c,t} \bar{q}'^U_{\alpha R} \not{D} q'^U_{\alpha R} \\
& - \frac{1}{4} A_{\mu\nu} A^{\mu\nu} - \frac{1}{4} B_{\mu\nu} B^{\mu\nu} \\
& + (D_\rho \Phi)^\dagger (D^\rho \Phi) - \mu^2 \Phi^\dagger \Phi - \lambda (\Phi^\dagger \Phi)^2 \\
& - \sum_{\alpha,\beta=e,\mu,\tau} \left( Y_{\alpha\beta}^n \bar{L}'_{\alpha L} \Phi l'_{\beta R} + Y_{\alpha\beta}^{n*} \bar{l}'_{\beta R} \Phi^\dagger L'_{\alpha L} \right) \\
& - \sum_{\alpha=1,2,3} \sum_{\beta=d,s,b} \left( Y_{\alpha\beta}^D \bar{Q}'_{\alpha L} \Phi q'^D_{\beta R} + Y_{\alpha\beta}^{D*} \bar{q}'^D_{\beta R} \Phi^\dagger Q'_{\alpha L} \right) \\
& - \sum_{\alpha=1,2,3} \sum_{\beta=u,c,t} \left( Y_{\alpha\beta}^U \bar{Q}'_{\alpha L} \tilde{\Phi} q'^U_{\beta R} + Y_{\alpha\beta}^{U*} \bar{q}'^U_{\beta R} \tilde{\Phi}^\dagger Q'_{\alpha L} \right). \tag{1.7}
\end{aligned}$$

The first two lines of the lagrangian summarize the kinetic terms for the fermionic

fields and their coupling to the gauge bosons  $A_a^{\mu\nu}$ ,  $B^{\mu\nu}$ <sup>1</sup>. The third line describes the kinetic terms and the self-coupling terms of the gauge bosons. The forth line is the Higgs lagrangian, which results in the spontaneous symmetry breaking. The last three lines describe the Yukawa coupling between fermions and the Higgs field, origin of the fermions' mass.

The coupling between left-handed and right-handed field generates the mass term for fermions. The SM assumes only left-handed components for neutrinos, thus implying zero neutrino mass. Since any linear combination of massless fields results in a massless field, the flavor eigenstates are identical to the mass eigenstates in the SM.

### 1.2.2 Neutrino Oscillations

The determination of the flavor of a neutrino dynamically arises from the corresponding charged lepton associated in a change current interaction; for example, a  $\nu_e$  is a neutrino which produces an  $e^-$ , a  $\bar{\nu}_\mu$  is a neutrino which produces a  $\mu^+$ , *etc.* The neutrino flavor eigenstates  $|\nu_\alpha\rangle$ , with  $\alpha = e, \mu, \tau$ , are orthogonal to each other and form a base for the weak interaction matrix.

Overwhelming experimental data show neutrinos change flavor during their propagation [83]. This phenomenon, called “neutrino oscillations”, was predicted first by Bruno Pontecorvo in 1957 [84]. Neutrino oscillations are possible only if the neutrino flavor eigenstate are not identical to the mass eigenstates, thus resulting in the first evidence of physics beyond the Standard Model. A minimal extension of the SM introduces three mass eigenstates,  $|\nu_i\rangle$  ( $i = 1, 2, 3$ ), whose mass  $m_i$  is well defined. The unitary Pontecorvo-Maki-Nakagawa-Sakata matrix transforms the spinor wave functions ( $\psi$ ) of each component between the flavor and mass bases as follows

---

1. In gauge theories the ordinary derivative  $\partial_\mu$  is substituted with the covariant derivative  $D_\mu$ . Here  $D_\mu = \partial_\mu + igA_\mu \cdot I + ig'B_\mu \frac{Y}{2}$ , where I and Y are the SU(2)<sub>L</sub> and U(1)<sub>Y</sub> generators, respectively.

$$\sum_{\alpha} \psi_{\alpha} |\nu_{\alpha}\rangle = \sum_i \psi_i |\nu_i\rangle, \rightarrow \psi_{\alpha} = U_{PMNS} \psi_i, \quad (1.8)$$

with

$$U_{PMNS} = \begin{bmatrix} c_{12} & s_{12} & 0 \\ -s_{12} & c_{12} & 0 \\ 0 & 0 & 1 \end{bmatrix} \begin{bmatrix} c_{13} & 0 & s_{13} e^{-i\delta} \\ 0 & 1 & 0 \\ -s_{13} e^{-i\delta} & 0 & c_{13} \end{bmatrix} \begin{bmatrix} 1 & 0 & 0 \\ 0 & c_{23} & s_{23} \\ 0 & -s_{23} & c_{23} \end{bmatrix} \begin{bmatrix} e^{i\alpha_1} & 0 & 0 \\ 0 & e^{i\alpha_2} & 0 \\ 0 & 0 & 1 \end{bmatrix} \quad (1.9)$$

where  $c$  e  $s$  stand respectively for cosine and sine of the corresponding mixing angles ( $\theta_{12}$ ,  $\theta_{23}$  and  $\theta_{13}$ ),  $\delta$  is the Dirac CP violation phase,  $\alpha_1$  and  $\alpha_2$  is the eventual Majorana CP violation phases. Experimental results on neutrino oscillations are generally reported in terms of the mixing angles and of the squared mass splitting  $\Delta m_{ab}^2 = m_a^2 - m_b^2$ , where  $a$  and  $b$  represent the mass eigenstates. A summary of the current status of experimental results, albeit partial, is given in table 1.2.

Table 1.2: Summary of experimental results on neutrino oscillation parameters. **ADD CITATIONS**

	Value	Precision	Experiment
$\theta_{23}$	$45^\circ$	9.0%	Super Kamiokande, MINOS,
$\Delta m_{23}^2$	$2.5 \cdot 10^{-3} \text{ eV}^2$	1.8%	No $\nu$ a, MACRO
$\theta_{12}$	$34^\circ$	5.8%	SNO, Gallex,
$\Delta m_{12}^2$	$7.4 \cdot 10^{-5} \text{ eV}^2$	2.8%	SAGE, KamLAND
$\theta_{13}$	$9^\circ$	4.7%	DAYA Bay,
$\Delta m_{13}^2$	$2.5 \cdot 10^{-3} \text{ eV}^2$	1.8%	RENO

### 1.2.3 Make up of Neutrino Interactions

All neutrino experiments involving the detection of single neutrinos are concerned with neutrino interactions (and neutrino cross sections) on nuclei. Given the invisible nature of the neutrino, characterizing the products of its interaction is the only

method to a) assess the neutrino presence, b) detect its flavor in case of a charge current interaction and c) eventually reconstruct its energy.

Historically, neutrino interactions with the nucleus in the GeV region are divided into three categories as a function of increasing neutrino energy: quasi elastic (QE), resonant, and deep inelastic (DIS) scattering. All current and forthcoming oscillation experiments live in the 0.1-10 GeV transition region, which encompasses the energy where the QE neutrino-nucleus interaction transitions into resonant scattering and the energy where resonance scattering transitions into DIS. Schematically, neutrino and antineutrino QE charge current scattering refers to the process  $\nu_l n \rightarrow l^- p$  and  $\bar{\nu}_l p \rightarrow l^+ n$  where a charged lepton and single nucleon are ejected in the elastic interaction, leaving the target nucleus in its ground state. Resonant scattering refers to an inelastic collision producing a nucleon excited state ( $\Delta, N^*$ ) – the resonance, indeed – which then quickly decays, most often to a nucleon and single-pion final state. DIS refers to the head-on collision between the neutrino and a parton inside the nucleon, producing hadronization and subsequent abundant production of mesons and nucleons. In addition to such interactions between the neutrino and a single component of the nucleus, neutrinos can also interact with the nucleus as a whole, albeit more rarely, a well documented process called coherent meson production scattering [46]; the signature of such process is the production of a distinctly forward-scattered single meson final state, most often a pion. This simple picture of neutrino interactions works rather well for scattering off of light nuclear targets, such as the H<sub>2</sub> and D<sub>2</sub> of bubble chamber experiments [51], but the complexity of the nuclear structure for heavier nuclei such as argon complicates this model.

As we will discuss in Chapter 2, the properties of argon make it a good candidate for interacting medium in neutrino experiments; in particular the density of its interaction centers augments the yield of neutrino interactions and allows for relatively compact detectors. Though, the choice of a relatively heavy nuclear target comes at

the cost of enhancing nuclear effects which modify the kinematic and final state of the neutrino interaction products.

Nuclear effects can potentially affect the neutrino event rates, nucleon emission, neutrino energy reconstruction, and the neutrino/antineutrino ratios, carrying deep implications for oscillation experiments. Even in the case of “simple” QE scattering, intra-nuclear hadron rescattering and correlation effects between the target nucleons can cause the ejection of additional nucleons in the final state, modifying the final state kinematics and topology. In case of resonant and DIS scattering, the hadronic interactions of meson and nucleons produced in the decay of the resonance or during hadronization complicate this picture even more. A large source of uncertainty in modeling nuclear effects in neutrino interactions come from mesons interactions (and re-interactions) in the nucleus, e.g., pion re-scattering, charge exchange, and absorption.

A renewed interest for neutrino cross section measurements surged in recent years, along with a lively discussion on the data reporting; the historical method of reporting the neutrino cross section as a function of the neutrino energy or momentum transferred shakes under the weight of its dependency on the chosen nuclear model. On one hand, correcting for nuclear effects in neutrino interaction can introduce unwanted sources of uncertainty and model dependency especially due to the mis-modeling of the meson interactions. On the other, avoiding this correction makes a comparison between neutrino interactions on different target nuclei extremely difficult.

Data on neutrino scattering off many different nuclei are available for both charged current (CC) and neutral current (NC) channels, as summarized in [51]. A summary of the results on QE, resonant and DIS scattering for neutrinos and antineutrinos from accelerators on different target is reported in Figure 1.1, where the (NUANCE) [28] event generator is used as comparison with the theory.

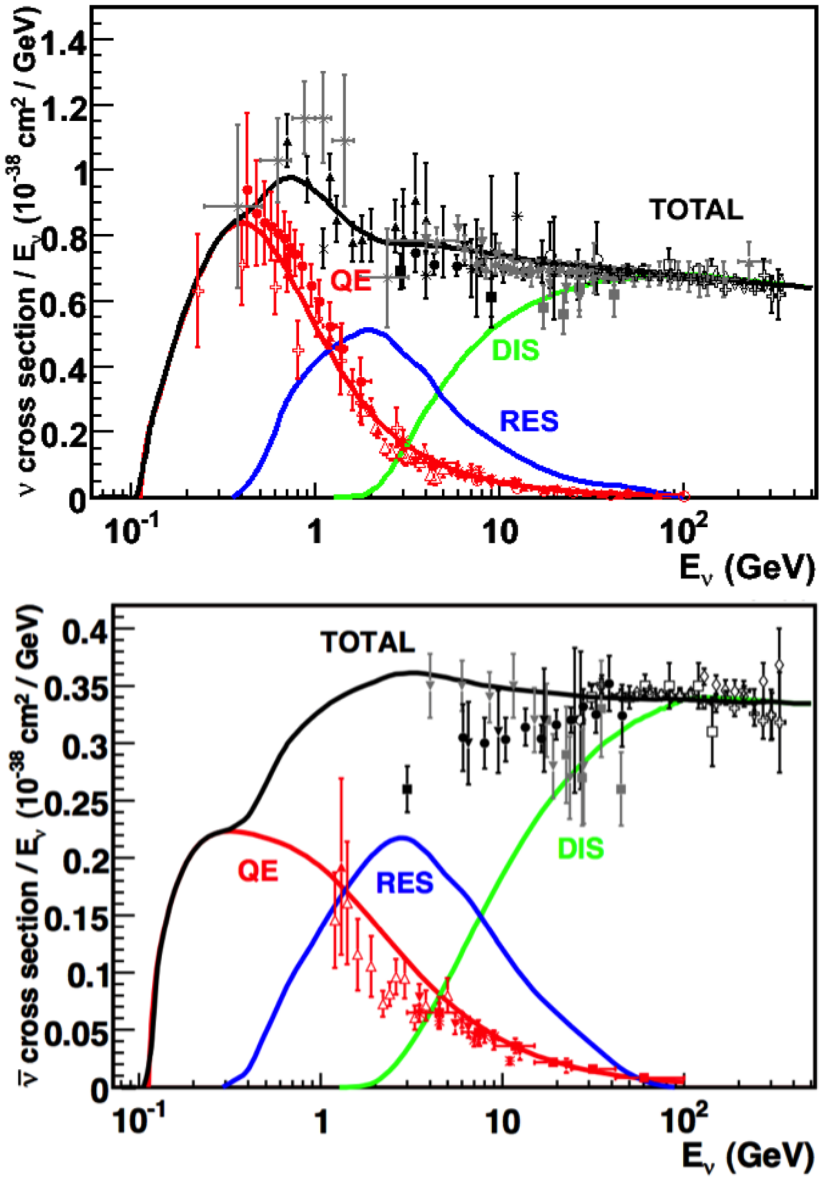


Figure 1.1: Total neutrino (top) and antineutrino (bottom) CC cross sections per nucleon divided by neutrino energy as a function of energy as reported in [51]. Predictions for the total (black), the QE (red), resonant (blue) and DIS (green) are provided by the NUANCE generator. The quasi-elastic scattering data and predictions have been averaged over neutron and proton targets (isoscalar target).

## 1.3 Beyond the Standard Model

The discovery of neutrino oscillation and its implication of non-zero neutrino mass mark the beginning of a new, exciting era in neutrino physics: the era of physics Beyond the Standard Model (BSM) at the intensity frontier. We are currently searching for new, deeper theories that can accommodate neutrinos with tiny but non-zero masses, while remaining consistent with the rest of the Standard Model.

### 1.3.1 Open Questions in Neutrino Physics

On one hand, the last three decades of experiments in neutrino oscillations brought spectacular advancements in the understanding of the oscillations pattern, measuring the neutrino mixing angles and mass splitting with a precision of less than 10%. On the other, it opened the field for a series of questions needing experimental answers.

**Sterile neutrinos.** Hints to the existence of at least one additional neutrino, in the form of various anomalies, have been puzzling physicists almost from the beginning of neutrino oscillation searches. Originally designed to look for evidence of neutrino oscillation, the Liquid Scintillator Neutrino Detector (LSND) [44] provided a first conflicting result with the Standard Model expectation of only three neutrinos. A second conflicting result has also been provided by the MiniBooNE experiment [40]. The LSND and MiniBooNE  $\nu_e$  and  $\bar{\nu}_e$  appearance results, known as the “LSND and MiniBooNE anomalies” [10, 11, 18], may be interpreted under the assumption of a new right-handed neutrino. The additional neutrino needs to be “sterile”, i.e needs not to couple with the electroweak force carriers, in order to meet the constraint imposed by the measurement of the width of the Z boson [1]. The new sterile neutrino would mainly be composed of a heavy neutrino  $\nu_4$  with mass  $m_4$  such that  $m_1, m_2, m_3 \ll m_4$  and  $\Delta m^2 = \Delta m_{14}^2 \sim [0.1 - 10] \text{ eV}^2$ . The introduction of sterile neutrinos is an appealing line of thinking, since this renormalizable generalization of the SM has the

potential to impact long standing questions in high energy physics and cosmology: light sterile neutrinos are candidates for dark matter particles and there are ideas that the theory could be adjusted to explain the baryon asymmetry of the Universe via leptogenesis [56].

**CP Violation In Lepton Sector.** The measurement of non-zero value for the oscillation parameter  $\theta_{13}$  allows the exploration of low-energy CP violation in the lepton sector at neutrino long baseline oscillation experiments, enabling the possibility to measure the Dirac CP-violating phase  $\delta$ . Exciting theoretical results tie  $\delta$  directly to the generation of the baryon asymmetry of the Universe at the Grand Unified Theory scale [a couple of cit would be nice](#). According to the theoretical model described in [82], for example, leptogenesis can be achieved if  $|\sin \theta_{13} \sin \delta| > 0.11$ , i.e.  $\sin \delta > 0.7$ .

The asymmetry in the oscillation probability of neutrinos and antineutrinos is the observable sensitive to the Dirac CP-violating phase  $\delta$  leveraged in neutrino oscillation experiments. Using the parameterization of the PMNS matrix shown in Equation 1.9, the difference between the probability of  $\nu_e \rightarrow \nu_\mu$  oscillation and the probability of  $\bar{\nu}_e \rightarrow \bar{\nu}_\mu$  oscillation can be parametrized as follows [29],

$$P_{\nu_e \rightarrow \nu_\mu} - P_{\bar{\nu}_e \rightarrow \bar{\nu}_\mu} = J \cos \left( \pm \delta - \frac{\Delta_{31} L}{2} \right) \sin \left( \frac{\Delta_{21} L}{2} \right) \sin \left( \frac{\Delta_{31} L}{2} \right) \quad (1.10)$$

where

$$J = \cos \theta_{13} \sin 2\theta_{13} \sin 2\theta_{12} \sin 2\theta_{23} \quad (1.11)$$

is the Jarlskog invariant [64],  $L$  the neutrino baseline, i.e. the distance between the neutrino production and detection points, and  $\Delta_{ab}$  a factor proportional to the sign and magnitude of the mass splitting. From these equations, it is clear how the relative large value of  $\theta_{13}$  is a happy accident necessary not to completely suppress the sensitivity to CP violation. The equations also show how the sensitivity to  $\delta$  is tied

to the measurement of the least precisely measured mixing angle,  $\theta_{23}$  (via the  $\sin 2\theta_{23}$  term) and to an other unknown quantity, the neutrino “mass hierarchy” (via the  $\Delta_{ab}$  terms). The precise determination of  $\theta_{23}$  is often referred as to “the octant problem”. Current experimental results [2, 9] are consistent with  $\theta_{23} = 45^\circ$ , which would imply maximal mixing between  $\nu_\mu - \nu_\tau$ , hinting to an intriguing new symmetry. Therefore, a precise measurement of  $\theta_{23}$  is of great interest for theoretical models of quark-lepton universality [58, 75, 86], whose quark and lepton mixing matrices are proportional to the deviation of  $\theta_{23}$  from  $45^\circ$ .

**Neutrino mass hierarchy.** The “mass hierarchy” problem refers to the unknown ordering of the value of absolute mass of the neutrino mass eigenstates. Current oscillation experiments are sensitive only to the magnitude of the mass splitting, and not directly to its sign. In a framework where the lightest neutrino mass (arbitrarily) corresponds to the first eigenstate  $m_1$ , it is unknown whether  $m_2 - m_1 < m_3 - m_1$  (Normal Hierarchy) or  $m_2 - m_1 > m_3 - m_1$  (Inverted Hierarchy). The mass hierarchy affects not only the sensitivity to CP violation searches in long baseline oscillation experiments, but also the sensitivity to determine whether neutrinos are Majorana particles in neutrinoless double beta decay experiments.

**Majorana or Dirac?** Evidence of neutrino oscillations demands the introduction of a mechanism which can give mass to the neutrinos. This mechanism should possibly also explain why neutrino masses are at least six orders of magnitude lower than the electron mass (the second lightest SM fermion). In a description of neutrinos as Dirac 4-component spinors, the neutrino field acquires mass via the Higgs mechanism as any other fermion of the SM. In this case, the neutrino mass is given by  $m_a = \frac{y_a^\nu v}{\sqrt{2}}$ , where  $v$  is the Higgs VEV and  $y_a^\nu$  is the Yukawa coupling between the Higgs and the neutrino. The smallness of neutrino masses can only be pinned on a tiny Yukawa coupling which is not justified by the theory.

In 1937, Majorana demonstrated that the introduction of a two components spinor is

sufficient to describe a massive fermion [74]. The Dirac equations of motion for the chiral fields (equations 1.5 and 1.6) hold true in the case of two components spinor under the assumption that the chiral components  $\psi_R$  and  $\psi_L$  are correlated through the charge conjugation matrix  $\mathcal{C}$ ,  $\psi_R = \mathcal{C}\bar{\psi}_L$ . Therefore the theory is applicable only to neutral fermions. Neutrinos are the only neutral elementary particles in the SM – the only possible Majorana particle candidate. This theory constructs a neutrino Majorana mass term  $\mathcal{L}_5$  of the following form in the Higgs unitary gauge

$$\mathcal{L}_5 = \frac{1}{2} \frac{gv^2}{\mathcal{M}} \nu_L^T \mathcal{C}^\dagger \nu_L, \quad (1.12)$$

where  $g$  is the coupling coefficient,  $v$  the Higgs VEV and  $\mathcal{M}$  a constant with the dimension of the mass proportional to the scale of new physics. The  $\mathcal{L}_5$  term would introduce a non-renormalizable term in the lagrangian, since it has dimensions of energy to the fifth power. This is not allowed in the SM lagrangian; however, the existence of such terms is plausible if we consider the SM as an effective theory at low energy, manifestation of the symmetry breaking of a more general theory at higher energy, e.g. a Grand Unified Theory (GUT), and not the definitive theory. The mass term in eq 1.12 implies the neutrino mass to be  $m = \frac{gv^2}{\mathcal{M}}$ . The coupling coefficient can be of the order of any other fermion's coupling coefficient, since the smallness of neutrino masses is achieved by the big value of the new physics mass scale alone. This vanilla formulation is the conceptual basis for many flavors of *see-saw mechanism* [100], which we will not discuss here in any detail. However, it is fascinating how the puzzle of the neutrino mass hints to the existence of a deeper and more complete theory.

From a kinematic point of view, Dirac and Majorana neutrinos satisfy the same energy-momentum dispersion relationship. Thus, it is impossible to discern the neutrino nature through kinematic effects such as neutrino oscillations. Neutrinoless

double beta decay searches are the most promising way to understand the nature of the neutrino and are therefore subject of great theoretical and experimental interest. Observation of the lepton number violating process  $0\nu\beta\beta$  would imply neutrinos have a Majorana component. Depending on the mass hierarchy, the theory also predicts  $0\nu\beta\beta$  exclusion regions and confirmation of the sole Dirac component for neutrinos [34].

### 1.3.2 Towards a more fundamental theory: GUTs

Despite its highly predictive power, a number of conceptual issues arise in the SM which disfavor it to be a good candidate for a fundamental theory.

The SM does not include a suitable dark matter candidate and a mechanisms that accounts for the baryon asymmetry of the universe. Additionally, up to a total of 25 parameters remain seemingly arbitrary and need to be fitted to data: 3 gauge couplings, 9 charged fermion masses, 3 mixing angles and one CP phase in the CKM matrix, the Higgs mass and quartic coupling,  $\theta_{QCD}$ , 3 neutrino mixing angles, 1 Dirac phase and, eventually, 2 Majorana phases.

From a group theory perspective, the SM has a rather complex group structure, where a gauge group is formed with the direct product of other three groups as shown in eq. 1.1. Drawing a parallel with the electroweak symmetry breaking mechanism, where the  $SU(2)_T \otimes U(1)_Y$  is recovered from  $U(1)_{EM}$ , an interesting line of simplification for the SM group structure would be to devise a similar mechanism where  $SU(3)_C \otimes SU(2)_T \otimes U(1)_Y$  is recovered from an hypothetical larger group. IS THIS CORRECT? Just as the electroweak unification becomes evident at energies higher than the Higgs VEV, a direct manifestation of Grand Unification Theories (GUTs) would occur at even higher energies.

As the smallness of neutrino masses suggests the existence of a higher mass scale,

an other, even stronger, hint to Grand Unification comes from the slope of running of the coupling constants. The coupling constants for the electromagnetic, weak and strong interactions in the SM vary as a function of the interaction energy as shown in figure 1.2; they do not exactly meet under the current experimental constraints, but their trend is interesting enough to push for the construction of theories where perfect unification is achieved through the addition of new particles.

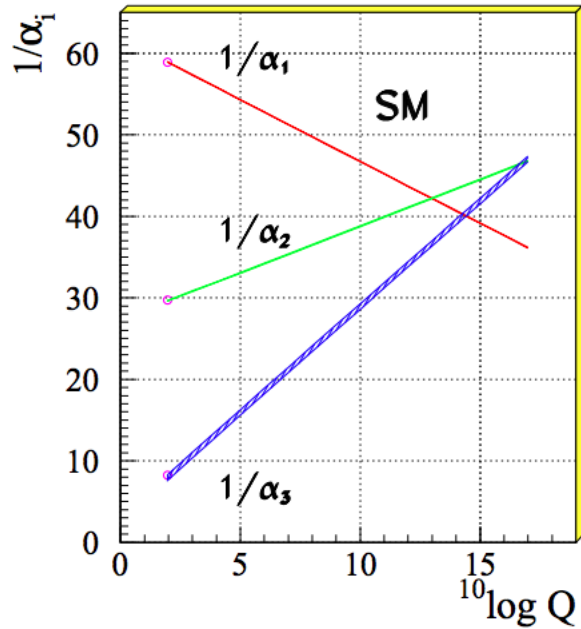


Figure 1.2: Evolution of the inverse of the three coupling constants in the Standard Model as a function of the momentum transferred, [68].

**SU(5).** The smallest simple group containing  $SU(3)_C \otimes SU(2)_T \otimes U(1)_Y$  is SU(5), as shown first by Georgi and Glashow in [54]. Quarks and leptons in this group fit the  $\bar{5}$  and 10 representations. The representation for left-handed fermions are the following

$$\bar{5} = (\nu_e, e^-)_L + \bar{d}_L \quad (1.13)$$

$$10 = e_L^+ + \bar{u}_L + (u, d)_L, \quad (1.14)$$

while the boson structure gains a new couple of super heavy bosons (X,Y)

$$24 = \underbrace{(8, 1)}_{\text{gluons}} + \underbrace{(1, 3) + (1, 1)}_{W^\pm, Z, \gamma} \dots + \underbrace{(3, 2) + (\bar{3}, 2)}_{X, Y \text{ bosons}}. \quad (1.15)$$

Nice features such as charge quantization and the identity between the positron and proton charge value come directly from the group structure. The new super heavy bosons are colored and form a weak doublet. Their are the mediator of the interaction that turns quarks into leptons, leading to predict the existence of processes that violate baryon number, such as  $p \rightarrow \pi^0 + e^+$  (see fig 1.8, right). The prediction for proton decay lifetime,  $\tau_p \sim \frac{M_X^4}{m_p^5} \sim 10^{30 \pm 1.5}$  years, is unfortunately experimentally disproved by IMB and Super-Kamiokande [?].

**SO(10).** More complicated group structures, such as SO(10) are still viable candidates for GUT. SO(10) includes the same type of  $X$  and  $Y$  bosons as SU(5). Right-handed massive neutrinos are embedded in the construction of the irreducible representation of SO(10). Different patterns of SO(10) symmetry breaking to recover the SM are possible and lead to different predictions for the proton decay lifetime; some of these predictions are not excluded by the experiments [69].

**SUSY GUTs.** Supersymmetry theories allow for another family of GUTs [?]. In SUSY, every fundamental particle in the SM has a “superpartner”, identical in each quantum number except for the spin-statistics: the fermion supersymmetric partners are bosons and vice versa. Collider experiments (mainly LHC) constrain the mass of the supersymmetric partners to be very heavy [?]. The SU(5), SU(10) groups with a SUSY twist are the basic groups for SUSY GUTs. From the phenomenology point of view, SUSY models tend to push the proton decay life time higher by a factor of four, they solve the “hierarchy problem”, and they also predict new channels for the proton decay. In particular they predict the presence of kaons in the final product, with a dominant mode of  $p \rightarrow \bar{\nu} K^+$ . Predictions on the proton decay lifetime depend

on the chosen SUSY model; again, some of the predictions are not excluded by the experiments [72, 73, 90].

## 1.4 Motivations for Hadronic Cross Sections in Argon

Critical challenges await the next decade of experimental physics at the intensity frontier. Following the recommendation of the latest Particle Physics Project Prioritization Panel [87], the US is dedicating substantial resources to the development of a short- and long- baseline neutrino program to address many of open questions in neutrino physics today. This program pivots on the Liquid Argon Time Projection Chamber (LArTPC) detector technology which will be described in Chapter 2.

The main goals of these research programs include:

- the assessment of the existence of right-handed sterile neutrinos via the study of accelerator neutrinos on a short baseline (SBN),
- the determination of the sign of  $\Delta m_{13}^2$  (or  $\Delta m_{23}^2$ ), i.e., the neutrino mass hierarchy via the study of accelerator neutrinos on a long baseline (DUNE),
- the determination of the octant, i.e. whether  $\theta_{23}$  is maximal, via the study of accelerator neutrinos on a long baseline (DUNE),
- the determination the status of CP symmetry in the lepton sector, via the study of accelerator neutrinos on a long baseline (DUNE),
- the search for observables predicted by GUTs, such as proton decay via the study of non accelerator physics in massive underground detectors (DUNE).

### 1.4.1 Pion-Argon Total Hadronic Cross Section

This section outlines the importance of the pion-argon total hadronic cross section in the context of the current and upcoming liquid argon neutrino experiments, SBN and DUNE. We describe the signal signature and historical measurements of pion-nucleus cross section, as well as the implementation of this cross sections in the current version of the simulation package used by LArIAT.

#### $\pi^-$ Ar Cross Section in the Context of Neutrino Searches

As outlined in 1.2.3, neutrino experiments use the products of neutrino interactions to identify the energy and flavor of the incoming neutrino. Pions are a common product of neutrino interaction, especially in resonant scattering, DIS and coherent pion production. For neutrino experiments in argon, there are two main reasons why understanding pion hadronic interactions with argon is important: to model the behavior of the pion inside the nucleus struck by the neutrino and to model the behavior of the pion during its propagation inside the detector medium.

Assumptions on the nuclear models and on the interaction of hadrons inside the nucleus performed at the level of the neutrino event generator bridge the measurement of the products of a neutrino interaction to the reconstruction of the neutrino energy and flavor. Thus, understanding pion hadronic interactions with the nucleus is particularly important to model correctly resonant, DIS and coherent pion production in neutrino interactions, where the presence of pions in the nucleus is abundant. For example, in case of resonant scattering,

$$\nu_l + N \rightarrow l + \Delta/N^* \rightarrow l + \pi + N', \quad (1.16)$$

the  $\Delta$  and  $N^*$  and excited states will decay hadronically in matters of  $\sim 10^{-24}$  s inside the nucleus producing pions which will bounce within the nuclear medium. The decay

modes for the lower mass  $\Delta$  (1232) and  $N^*(1440)$  are listed in table 1.3.

We illustrate here the basis of the GENIE Neutrino Generator [14], since it is one the most popular event generators for LAr experiments.

The key elements of a neutrino event generators for resonance and DIS events are the nuclear model and the hadron treatment (both production and transportation). We illustrate here the conceptual basis of the GENIE Neutrino Generator [14] as an example, since GENIE is one the most popular event generators for LAr experiments. For example, the nuclear model used by GENIE for all processes is a relativistic Fermi gas (RFG) modified to incorporate short range nucleon-nucleon correlations [23]. This means that the initial momentum and binding energy of the struck nucleon is determined by assuming nucleons inside the nucleus are quasi-free, acting independently in the mean field of the nucleus. For  $A > 20$  like argon, the 2-parameter Woods-Saxon shell model for density function is used. The GENIE module INTRANUKE [67] is used to simulate the final-state interactions (FSI) which is the hadron re-interaction inside the nucleus. This module places the outgoing particles in the nucleus and propagates them using the “hA model”. In the INTRANUKE hA model, hadrons can undergo at most one FSI per event. When possible, external hadron-nucleus scattering data are used to tune INTRANUKE. Since no data is available for Argon, GENIE uses an interpolation of data from heavier and lighter nuclei for the pion-argon cross section leading to big uncertainties in the INTRANUKE module.

Once the pion has left the target nucleus, the pion-argon hadronic cross section plays an important role in the pion transportation inside the argon medium: processes like pion absorption with emission of nucleons or pion charge exchange can greatly modify the topology of a neutrino interactions in the detector and lead to errors in the event classification. Being able to reconstruct the details of pions inside the detector is an imperative for modern liquid argon neutrino experiment to achieve the design resolution for their key physics measurements.

## $\pi^-$ -Ar Hadronic Interaction: Signal Signatures

Strong hadronic interaction models [39,55] predict the pion interaction processes with argon in the [100 - 1200] MeV energy range. The total hadronic  $\pi^-$ -Ar interaction cross section is defined as the one related to the single process driven only by the strong interaction which is dominant in the considered energy range. In measuring the “total” cross section, we include both the elastic and reaction channels, regardless of the final state,

$$\sigma_{Tot} = \sigma_{Elastic} + \sigma_{Reaction}; \quad (1.17)$$

the reaction channel is further characterized by several exclusive channels with defined topologies,

$$\sigma_{Reaction} = \sigma_{Inelastic} + \sigma_{abs} + \sigma_{chex} + \sigma_{\pi prod}. \quad (1.18)$$

A summary of the pion final states in order of pion multiplicity for the reaction channel is given in table 1.4. Pion capture and pion decay at rest dominate the cross section under 100 MeV. We define pion capture as the process determining the formation of a pionic atom and the subsequent pion’s end of life. Stopping negative pions can form pionic argon, where the negative pion plays the role of an orbital electron. Since the pion mass is two orders of magnitude greater than the electron mass, the spatial wave form of the pion will overlap way more with the nucleus compared to the electron case. After the electromagnetic formation of the pionic atom, the pion will quickly be absorbed by the nucleus, which is put in an excited state. The nucleus then de-excites with the emission of low energy nucleons and photons. Pion capture is predominant compared to pion decay, the other important process for very low energy pions. The decay of a pion is governed by the weak force; the pion decay life time is  $\tau_\pi = 2.6 \times 10^{-8}$  s and the main decay mode is  $\pi^- \rightarrow \mu^- + \bar{\nu}_\mu$  (BR 99.98%). Since pion capture can be considered an electromagnetic process and pion decay is a weak process, this energy region is purposely excluded from the hadronic

cross section measurement.

### Previous measurements: Lighter and Heavier Nuclei

Many experiments with pion beams have studied the hadronic interaction of pions on light and heavy materials, such as He, Li, C, Fe, Pb [27]. However, data on argon are rare: the total differential hadronic cross section has never been measured before on argon. Simulation packages like Geant4 base their pion transportation for argon on data from lighter and heavier nuclei: the goal of LArIAT’s dedicated measurement on argon is to bridge this gap in data, thus reducing the uncertainties related to pions interaction in argon in both neutrino event generators and in simulation packages of pion transportation.

The shape of the pion-nucleus interaction cross section in the energy range considered shows the distinct features that indicate the presence of a resonance. In fact, the mean free path of a pion of kinetic energy between 100 and 400 MeV is much shorter than the average distance between nucleons (which is of the order of 1 fm). Therefore, the pion interacts with surface nucleons. A  $\Delta$  resonance is often produced in the interaction, which subsequently decays inside the nucleus. Experimental results on several nuclei as reported in [27] are shown in Figure 1.3; it is interesting to notice here how the shape of the  $\Delta$  resonance become less pronounced as a function of the mass number of the target nucleus. Pion interactions with heavier nuclei also shift the peak of the resonance at lower energy; this effect is due to kinematic considerations and to the difference in propagation of the  $\Delta$  inside the nucleus. Multiple scattering effect modify the resonance width, which is larger than the natural-decay width. As an example of a fairly well studied target, Figure 1.4 reports the negative pion cross section on Carbon for the elastic and reaction<sup>2</sup> channels, and their sum [45].

---

2. This paper calls “inelastic interaction” what we refer as to “reaction channel”.

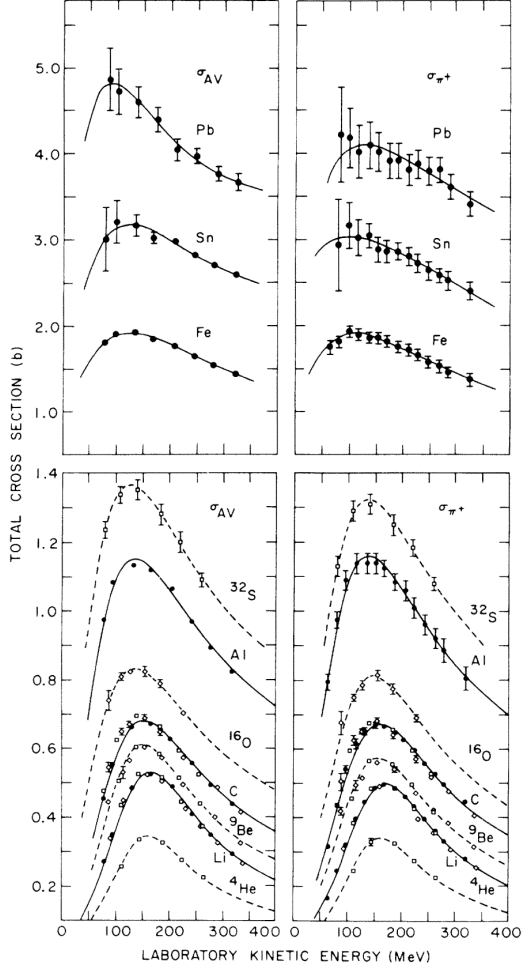


Figure 1.3: Pion-nucleus total cross sections:  $\sigma_{\pi^+}$  for positive pions (right) and  $\sigma_{AV}$  (left) for the average between positive and negative pions  $\sigma_{AV} = \frac{\sigma_{\pi^+} + \sigma_{\pi^-}}{2}$  in the  $\Delta$  resonance region. The error bars include estimates of systematic uncertainties. The curves are the results of fits to the data assuming a Breit-Wigner shape. This summary plot is reported in [27] and uses data from [42, 96].

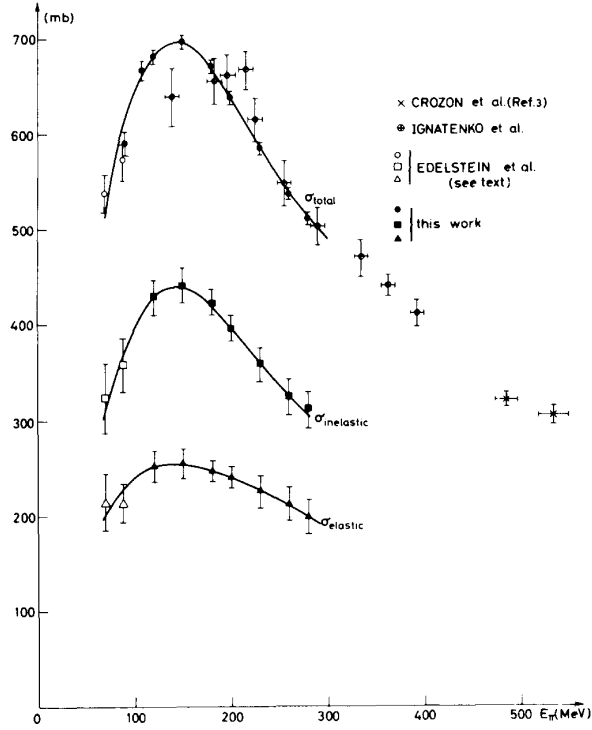


Figure 1.4: Negative pion nucleus total, elastic and reaction cross sections on  $^{12}\text{C}$  as from [45].

### Negative Pion Interaction Cross Section in Simulation Packages

LArIAT uses Geant4 as the default simulation package. In particular, pions (and kaons) transportation is achieved through the Geant4 FTFP\_BERT physics list. In this physics list, Geant4 uses the Bertini cascade model [97] to simulate the products of the pion-nucleus interaction as well as the secondary hadrons re-interactions inside the target nucleus (intra-nuclear cascade). The target nucleus is represented as a continuous gas where the nuclear potential follows concentrical shells whose depths approximate the Woods-Saxon shape. The CERN-HERA compilations [93, 94] of hadron-nucleon interaction data is the data base used for the decision making process after the cascade is invoked. The cross section model determines if the pion interacts, the eventual type of interaction and the interaction multiplicity. For hadron projectiles with energy less than 20 GeV, Geant4 reports the uncertainty on the cross

section model to be about the size of the error bars on the data used, or about 10%, increasing to 20-30% in energy regions where data is sparse.

The relevance of the GENIE generator for neutrino physics and its basic working principles have been outlined earlier in this section. Given GENIE’s modularity, information on hadron-nucleus interactions can be extracted from the INTRANUKE module and directly compared against the Geant4 predictions.

The work in [79] reviews the current status of negative and positive pion simulation in Geant4 and GENIE for  $^{12}\text{C}$ ,  $^{56}\text{Fe}$ , and  $^{40}\text{Ca}$ . From that work, we report the results for  $^{12}\text{C}$  in Figure 1.5 as it allows a direct comparison between Geant4, GENIE and data. Geant4 predictions for  $\pi^-$  on Carbon are in good agreement with data over all the spectrum, while GENIE predictions seem to show some features at around 500 MeV and 900 MeV, maybe due to higher resonances in the hA model. From the same work, we also report the negative pion cross section on  $^{40}\text{Ca}$  in Figure 1.6, since this is the nuclear medium closest argon with some available data. The predictions from both Geant4 and GENIE agree with data in the high energy region; the Geant4 and GENIE predictions diverge in the resonance region, where data is not available. These few examples highlight how cross section data for the specific nucleus considered in the neutrino experiments is fundamental to inform the Monte Carlo simulation.

For the  $\pi^-$  argon total cross section measurement, we use the Geant4 Bertini Cascade model, whose predictions for the total, elastic and reaction cross sections are show in Figure 1.7.

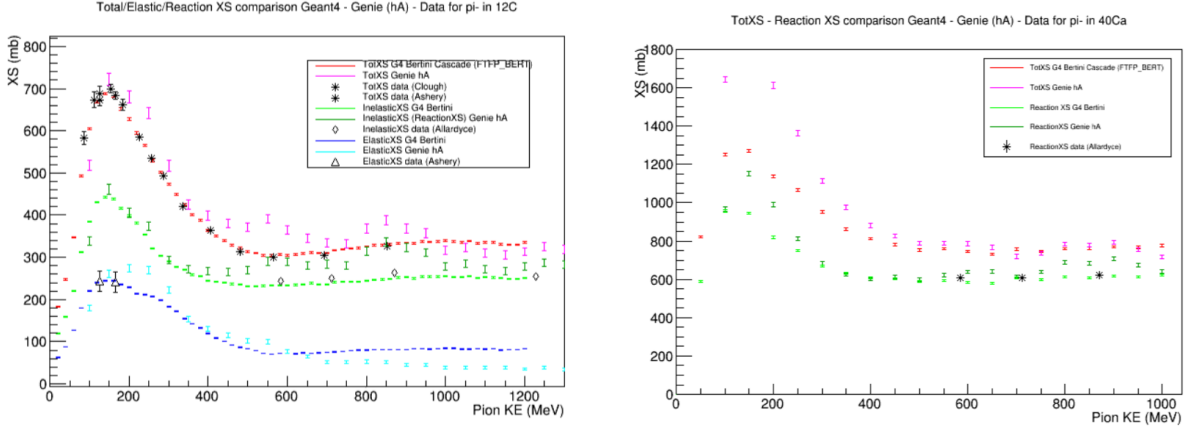


Figure 1.5: Total, elastic and reaction cross section for  $\pi^-$  on  $^{12}\text{C}$ . Comparison between results from Geant4 simulation (Bertini cascade model), Genie simulation (hA model), and experimental data [17, 42, 43, 89].

Figure 1.6: Total, elastic and reaction cross section for  $\pi^-$  on  $^{40}\text{Ca}$ . Comparison between results from Geant4 simulation (Bertini cascade model), Genie simulation (hA model), and experimental data [43].

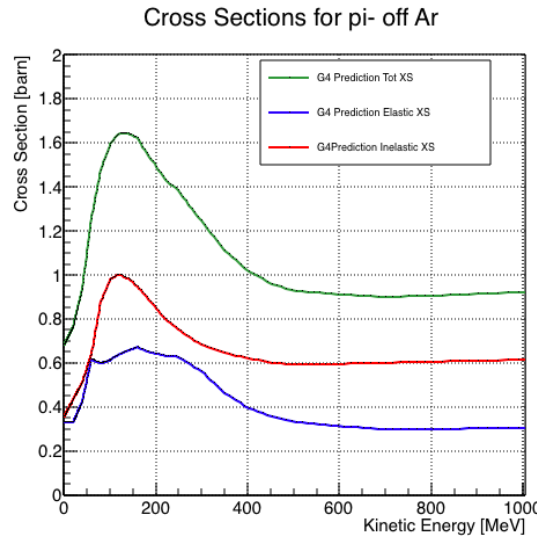


Figure 1.7: Total, elastic and reaction hadronic cross section for  $\pi^-$ -argon implemented in Geant4 10.01.p3.

Resonance	Decay Mode	Lifetime (s)
$\Delta$ (1232) $3/2^+$	$\Delta^{++}(\text{uuu}) \rightarrow p\pi^+$ $\Delta^+(\text{uud}) \rightarrow n\pi^+$ $\Delta^+(\text{uud}) \rightarrow p\pi^0$ $\Delta^0(\text{udd}) \rightarrow n\pi^0$ $\Delta^0(\text{udd}) \rightarrow p\pi^-$ $\Delta^-(\text{ddd}) \rightarrow n\pi^-$	$\sim 5.6 \times 10^{-24}$
$N^*$ (1440) $1/2^+$	$N^* \rightarrow N\pi$ $N^* \rightarrow N\pi\pi$	$\sim 2.2 \times 10^{-24}$

Table 1.3: Main decay modes of the lightest Delta resonance and Nucleon excited state.

N $\pi$ in FS	Channel Name	Reaction	Notes
0	Pion Absorption, $\sigma_{abs}$	$\pi^-(np) \rightarrow nn$ (2-body abs) $\pi^-(nnp) \rightarrow nnn$ (3-body abs) $\pi^-(npp) \rightarrow pnn$ (3-body abs) $\pi^-(nnpp) \rightarrow pmn$ (Multi-body abs)	Suppressed on single nucleon by energy conservation: the process occurs on at least two nucleons system.
1	Elastic Scattering, $\sigma_{el}$	$\pi^- + N \rightarrow \pi^- + N$	Scattering on nucleon or nucleus, the target is left in ground state
1	Charge Exchange, $\sigma_{chea}$	$\pi^- + p \rightarrow \Delta^0 \rightarrow \pi^0 + n$ $\pi^- + N \rightarrow \pi^+ +$ nucleons	Single charge exchange: charged pion converts into neutral pion  Double charge exchange: charged pion converts into opposite charge pion
1	Inelastic Scattering, $\sigma_{inel}$	$\pi^- + p \rightarrow \Delta^0 \rightarrow \pi^- + p$ (knock-out) $\pi^- + n \rightarrow \Delta^- \rightarrow \pi^- + n$ (knock-out)	Other possible reactions:  Pure Inelastic scattering: population of low energy bound excited states Nuclear break-up with nucleons or fragments knock-out
2+	Pion Production, $\sigma_{\pi prod}$	$\pi^- + N \rightarrow \geq 2\pi +$ nucleons	Possible if pion K.E $\geq 500$ MeV/c

Table 1.4: Summary of negative pion hadronic interactions of the reaction channel as a function of the pion multiplicity in the final state in the energy range [100-1200] MeV.

## 1.4.2 Kaon-Argon Total Hadronic Cross Section

This section outlines the importance of the kaon-argon total hadronic cross section. We start by discussing the measurement in the context of nucleon decay searches. We then describe the signal signature and historical measurements of kaon-nucleus cross section, as well as the implementation of this cross sections in the current version of the simulation package used by LArIAT.

### K<sup>+</sup>Ar Cross section in the Context of Nucleon Decay Searches

#### Nucleon decay

Baryon number is accidentally conserved in the Standard Model. Even though no baryon number violation has been experimentally observed thus far, no underlying symmetry in line with the Noether paradigm [78] explains its conservation. As shown in section 1.3.2, almost all Grand Unified Theories predict at some level baryon number violation in the form of nucleon decay on long time-scales. Given the impossibility to reach grand unification energy scales with collider experiments (Energy Scale  $> 10^{15}$  GeV), an indirect proof of GUTs is needed. The experimental observation of nucleon decay may be the only viable way to explore these theories.

In case of nucleon decay discovery, the dominant decay mode may uncover additional information about the GUT type. Supersymmetric GUTs [19, 36] prefer the presence of kaons in the products of the decay, e.g.  $p \rightarrow K^+ \bar{\nu}$  (see fig 1.8, left). Gauge mediated GUTs, in which new gauge bosons are introduced that allow for the transformation of quarks into leptons, and vice versa, prefer the mode  $p \rightarrow e^+ \pi^0$  (see fig 1.8, right).

LArIAT tiny active volume makes it impossible for the experiment to place competitive limits on nucleon decay searches. However, LArIAT provides excellent data to characterize kaons in liquid argon for the “LAr golden mode”,  $p \rightarrow K^+ \bar{\nu}$ . The

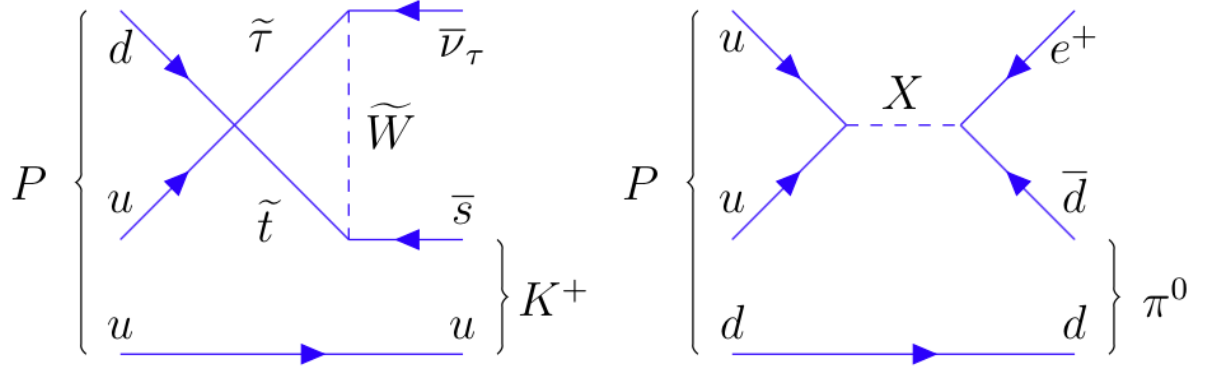


Figure 1.8: Feynman diagrams for proton decay “golden modes”:  $p \rightarrow K^+\bar{\nu}$  for supersymmetric GUTs on the left and  $p \rightarrow e^+\pi^0$  for gauge-mediated GUTs on the right.

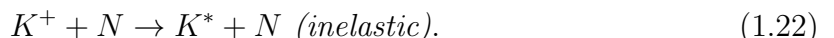
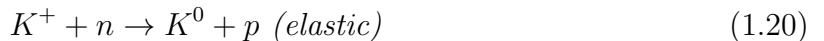
result of these studies will affect future proton decay searches in LArTPCs. Previous work has been done to assess the potential identification efficiency for different decay modes in a LArTPC [41], but, as the time of this writing, no study of kaon selection efficiency in LArTPCs has been performed on data. The  $K^+$ -Ar interaction cross section has never been measured before and can affect the possibility of detecting and measuring kaons when produced in a proton decay event. Kaon interactions with argon can distort the kaon energy spectrum as well as change the topology of single kaon events. In a LArTPC, non-interacting kaons appear as straight tracks with a high ionization depositions at the end (Bragg peak). The topology of interacting kaons can be quite different. In case of elastic scattering, a distinct kink will be present in the track. In case of inelastic scattering the Bragg peak will not be present and additional tracks will populate the event. Performing the total hadronic  $K^+$ -Ar cross section measurement on data serves the double purpose of identifying the rate of “unusual” topologies (kinks and additional tracks) and of developing tools for kaon tracking in LAr.

## **K<sup>+</sup>Ar Hadronic Interaction: Signal Signatures**

The interaction of a mildly relativistic charged kaon with an argon nucleus is determined largely by the strong force. The total hadronic K<sup>+</sup>-Ar interaction cross section is defined as the one related to the single (hadronic) process driven only by the strong interaction. In this case, “total” indicates all strong interactions regardless of the final state. This condition purposefully includes both elastic and inelastic (reaction) channels. Indeed, the total cross section section can be then decomposed into

$$\sigma_{Tot} = \sigma_{Elastic} + \sigma_{Reaction}.$$

For the LArIAT cross section analysis, the kaons considered span a momentum inside the TPC from 100 MeV/c to 800 MeV/c. In this energy range, the relevant K-Nucleon interactions are according to [50]:



## **Previous Measurements: Lighter and Heavier Nuclei**

In general, measurements on kaon cross sections are extremely scarce. The measurement of the kaon interaction cross section would bring the additional benefit of reducing the uncertainties associated with hadron interaction models adopted in MC simulations for argon targets, beneficial for both proton decay studies and kaon production from neutrino interaction studies, where the uncertainties for final state interaction models are big [37].

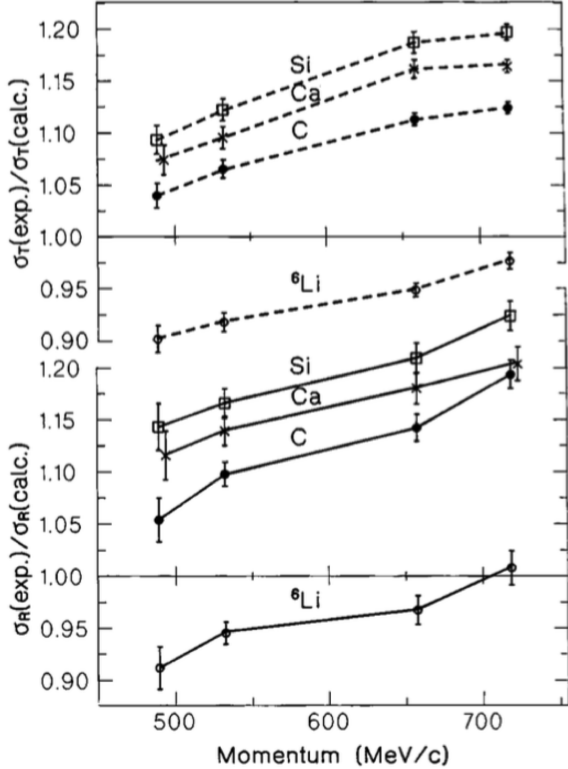


Figure 1.9: Ratios between experimental and calculated cross sections as from [52]. Top: Total cross sections. Bottom: reaction cross sections.

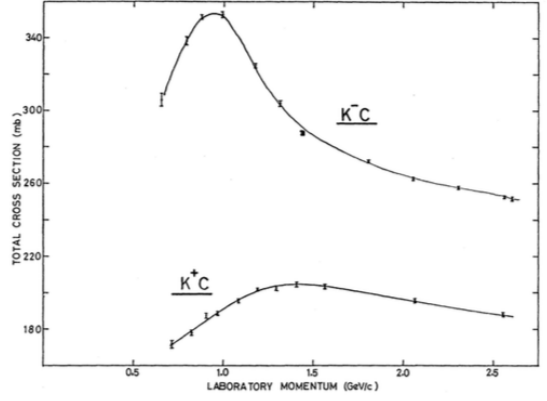


Figure 1.10: Total  $K^+$  and  $K^-$  cross sections on carbon as from [25].

Figure 1.9 shows a 1997 measurement on several elements as performed by Friedmann et al. [52]. As a reference, this paper measures a  $\sigma_{Tot}$  for Si of  $366.5 \pm 4.8$  mb and a  $\sigma_{Tot}$  for Ca of  $494.6 \pm 7.7$  mb at 488 MeV/c. The cross section for argon is expected to lie in between these two measurements. Additional data on the kaon cross section are provided by Bugg et al. [25]. Bugg performs a measurement of the total  $K^+$  and  $K^-$  cross sections on protons and deuterons over the range of 0.6-2.65 GeV/c, as well as a measurement of the total  $K^+$  and  $K^-$  cross sections on carbon for a number of momenta; the results of this paper on carbon are reported in Figure 1.10.

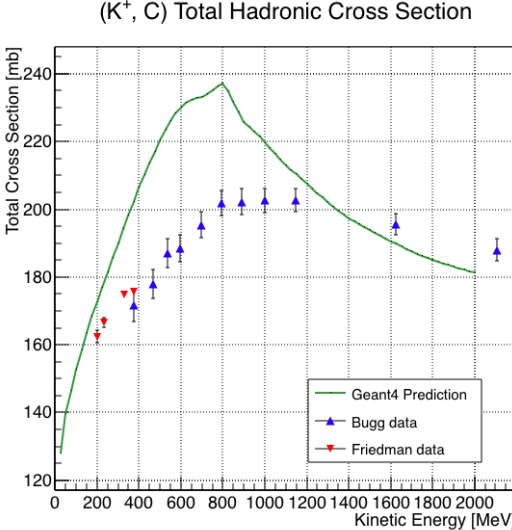


Figure 1.11: Total hadronic cross section for carbon implemented in Geant4 10.01.p3 with overlaid with the Bugg and Friedman data.

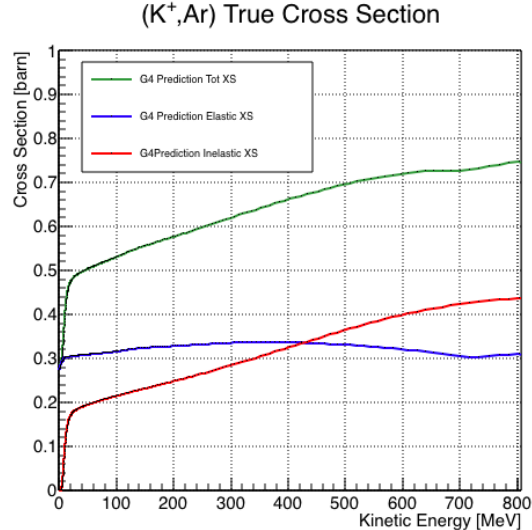


Figure 1.12: Total, elastic and reaction hadronic cross section for  $K^+$ -argon implemented in Geant4 10.01.p3.

### Kaon Interaction Cross Section for thin target in Geant4

Since the kaon cross section in argon has never been measured before, simulation packages tune kaon transportation in argon by extrapolation from lighter and heavier nuclei. LArIAT uses the Geant4 suite for particle transportation. Since kaon data on carbon are available, we used it as a metric to evaluate the Geant4 prediction performances. Figure 1.11 shows the total hadronic cross section for carbon implemented in Geant4 10.01.p3 overlaid with the Bugg and Friedman data. Unfortunately, the current version of Geant4 does not reproduce the data for carbon closely. On one hand, this evidence makes us even more wary when using the Monte Carlo in simulating the kaon-argon interactions. On the other, it further highlights the importance of the kaon measurement. Figure 1.12 shows the Geant4 prediction for the total, elastic and reaction cross section for  $K^+$  on argon.

# Chapter 2

## Liquid Argon Detectors at the Intensity Frontier

In the next few years, LArTPCs will be the tools to answer some of the burning questions in neutrino physics today. This section illustrates the operational principles of this detector technology, as well as the scope of the key detectors in the US liquid argon program – SBN, DUNE and LArIAT.

### 2.1 The Liquid Argon Time Projection Chamber Technology

#### 2.1.1 TPCs, Neutrinos & Argon

David Nygren designed the first Time Projection Chamber (TPC) in the late 1970s [80] for the PEP-4 experiment, a detector apt to study electron-positron collisions at the PEP storage ring at the SLAC National Accelerator Laboratory. From the original design in the seventies – a cylindrical chamber filled with methane gas – the TPC detector concept has seen many incarnations, the employment of several different active media and a variety of different particle physics applications, including, but

not limited to the study of electron/positron storage rings (e.g. PEP4, TOPAZ, ALEPH and DELPHI), heavy ions collisions in fixed target and collider experiments (e.g. EOS/HISSL and ALICE ), dark matter (ArDM), rare decays and capture (e.g. TRIUMF, MuCap), neutrino detectors and nucleon decay (ICARUS, SBN, DUNE), and neutrino less double beta decay (Next). A nice review of the history of TPCs and working principles is provided in [61].

Several features of the TPC technology make these detectors a more versatile tool compared to other ionization detectors and explain such a wide popularity. TPCs are the only electronically read detector which deliver simultaneous three-dimensional track information and a measurement of the particle energy loss. Leveraging on both tracking and calorimetry, particle identification (PID) capabilities are enhanced over a wide momentum range.

Historically, the active medium in ionization detectors has been in the gaseous form. Carlo Rubbia first proposed the use of a Liquid Argon TPC for a neutrino experiment, ICARUS [88], in 1977. Using nobles elements in the liquid form for neutrino detectors is advantageous for several reasons. The density of liquids is  $\sim$ 1000 times greater than gases, increasing the number of target centers for neutrino's interaction in the same volume. Since the energy loss of charged particle is proportional to the target material density, as shown in the Bethe-Block equation, eq. 2.1, the increased density reflects into a proportionally higher energy loss, enhancing the calorimetry capability of detectors with a liquid active medium. Additionally, the ionization energy of liquids is smaller than gasses by the order of tens of eV. Thus, at the passage of charged particles, liquid generally produce more ionization electrons than gas for the same deposited energy and force the particles to deposit more energy in a shorter range. The downside of using noble liquid gasses in experiments is that they require expensive cryogenic systems to cool the gas until it transitions to its the liquid form. The properties of liquid argon in comparison liquid xenon – a popular choice for

Element	LAr	LXe
Atomic Number	18	54
Atomic weight A	40	131
Boiling Point Tb at 1 atm	87.3 K	165.0 K
Density	1.4 g/cm <sup>3</sup>	3.0 g/cm <sup>3</sup>
Radiation length	14.0 cm	2.8 cm
Moliere Radius	10.0 cm	5.7 cm
Work function	23.6 eV	15.6 eV
Electron Mobility at $E_{field} = 10^4$ V/m	0.047 m <sup>2</sup> /Vs	0.22 m <sup>2</sup> /Vs
Average dE/dx MIP	2.1 MeV/cm	3.8 MeV/cm
Average Scintillation Light Yield	40000 $\gamma$ /MeV	42000 $\gamma$ /MeV
Scintillation $\lambda$	128 nm	175 nm

Table 2.1: LAr, LXe summary of properties relevant for neutrino detectors.

dark matter and neutrinoless double beta decay detectors – are summarized in table 2.1. Albeit xenon would be more desirable than argon given some superior properties such as lower ionization energy and higher density and light yield, argon relative abundance abates the cost of argon compared to xenon, making argon a more viable choice for the construction of kilo-ton scale neutrino detectors.

LArTPCs are some times referred as to “electronic” bubble-chambers, for the similarity in the tracking and energy resolution which is coupled with an electronic readout of the imaging information in LArTPCs. Compared to these historic detectors however, LArTPC bestow tridimensional tracking and a self triggering mechanism provided by the scintillation light in the noble gas. An event display of a  $\nu_\mu$  CC interaction candidate in the MicroBooNE detector is shown in picture 2.1 to display the level of spatial details these detectors are capable of; the color scale of the image is proportional to the energy deposited, hinting to the calorimetry capabilities of the detectors.

### 2.1.2 LArTPC: Principles of Operation

To the bare bones, a LArTPC is a bulk of liquid argon sandwiched in a flat capacitor, equipped with a light collection system. A uniform electric field of the order of

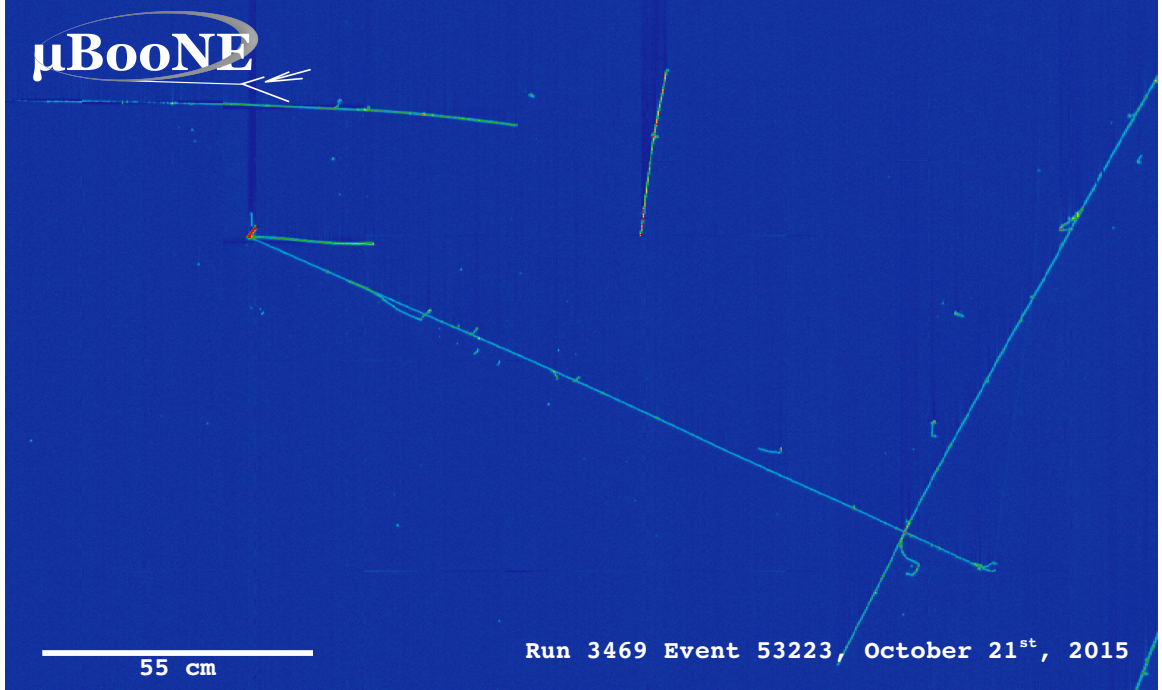


Figure 2.1: Event display of a  $\nu_\mu$  CC interaction candidate in the MicroBooNE detector.

500 V/cm is maintained constant between the faces of the capacitor. The anode is sensitive to ionization charge and it is usually made of two or more planes segmented into several hundreds parallel sense wires a few millimeters apart; different geometries for the anode segmentation are under study [38].

Argon ionization and scintillation are the processes leveraged to detect particles in the LArTPC active volume. When a ionizing radiation traverses the argon active volume it leaves a trail of ionization electrons along its trajectory and it excites the argon producing of scintillation light – details on the production and detection of ionization charge and scintillation light are provided in 2.1.4 and 2.1.4 respectively. The optical the detector sees the argon scintillation light in matters of nanoseconds. This flash of light determines the start time of an event in the chamber,  $t_0$ . The uniform electric field drifts the ionization electrons from the production point towards the anode in order of hundreds of microseconds or more depending on the chamber

dimensions<sup>1</sup>. The anode sense wires see either an induced current by the drifting charge (on induction planes) or an injection of the ionization charge (collection plane). An appropriate choice of the voltage bias on each wire plane assures ideal charge transparency, so that all the ionization charge is collected on the collection plane and none on the induction planes.

The arrival time of the charge on the anode sense wires is used to measure the position of the original ionizing radiation in the drift direction. In fact, since the constant electric field implies that the drift velocity is also constant, the position of the original ionization is simply given by the multiplication of the drift velocity by the drift time, where the “drift time” is the difference between  $t_0$  and the charge arrival time on the wire planes. The spacial resolution on this dimension is limited by the time resolution of the electronics or by longitudinal diffusion of the electrons. The spatial information on the different wire planes maps a bi-dimensional projection of the interaction pattern in the plane perpendicular to the drift direction. The spacial resolution on this dimension is limited by the transverse electron diffusion in argon and by the grain of the anode segmentation, i.e. the spacing between the wires in the sense planes [35]. The off-line combination of the 2-D information on the wire planes with the timing information allows for the 3D reconstruction of the event in the chamber.

Since the charge deposited by the ionizing radiation is proportional to the deposited energy and the charge collected on the sense plane is a function of the deposited charge, LArTPC allow the measurement of the energy deposit in the active volume. Effects due to the presence of free charge and impurities in the active volume, such as a finite electron lifetime, recombination and space charge, complicate

---

1. The ionized argon also drifts, but in the opposite directions compared to the electrons. Since the drift time is proportional to the particle mass, the ions’ drift time is much longer than the electrons’. Ionized argon is collected on the cathode which is not instrumented, so it is not used to infer information about the interactions in the chamber.

the relationship between deposited and collected charge affecting the measurement of the particle's energy, as described in the next section.

### 2.1.3 Liquid Argon: Ionization Charge

The mean rate of energy loss by moderately relativistic elementary charge particles heavier than electrons is well described by the modified Bethe-Bloch [83] equation

$$-\frac{dE}{dx} = K z^2 \frac{Z}{A} \varrho \frac{1}{\beta^2} \left[ \frac{1}{2} \ln \frac{2m_e c^2 \beta^2 \gamma^2 T_{max}}{I^2} - \beta^2 - \frac{\delta}{2} \right], \quad (2.1)$$

where  $z$  is the number of unit charge of the ionizing radiation,  $Z$ ,  $A$  and  $\varrho$  are the atomic number, mass number and density of the medium,  $m_e$  is the electron mass,  $\gamma = \frac{\beta}{\sqrt{1-\beta^2}}$  is the Lorentz factor of the ionizing radiation,  $T_{max}$  is the maximum kinetic energy which can be imparted to a free electron in a single collision,  $I$  is the mean excitation energy on eV,  $\delta$  is the density correction and  $K = 0.307075 \text{ MeV g}^{-1} \text{ cm}^2$  is a numerical conversion factor. The Bethe-Bloch treats the energy loss by an ionizing radiation via quantum-mechanical collisions producing ionization or an excitation in the medium as an uniform and continuous process. The density correction terms becomes relevant for incident particle with high energy, where screening effects due to the polarization of the medium by high energy particles occur.

Excitation and ionization of the detector medium occur in similar amounts. Since the ionizing collisions occur randomly, we can parametrize their number  $k$  in a segment of length  $s$  along the track with a Poissonian function

$$P(k) = \frac{s^k}{k! \lambda^k} e^{-s/\lambda}, \quad (2.2)$$

where  $\lambda = 1/N_e \sigma_i$ , with  $N_e$  being the electron density of  $\sigma_i$  the ionization cross-section per electron. About 66% of the ionizing collisions in Argon produce only a single electron/ion pair [61]; in the other cases, the transferred kinetic energy is enough

for the primary electron to liberate one or more secondary electrons, which usually stay close to the original pair. Occasionally, electrons can receive enough energy to be ejected with high energy, forming so-called “ $\delta$ -ray”: a detectable ionization short track off the particle trajectory, as shown in figure 2.2. The average number of  $\delta$ -ray with energy  $E > E_0$  per cm follows the empirical form

$$P(E > E_0) \sim \frac{y}{\beta^2 E_0}, \quad (2.3)$$

where  $y$  is an empirical factor depending on the medium (0.114 for gaseous Ar), and  $\beta$  is  $v/c$ .

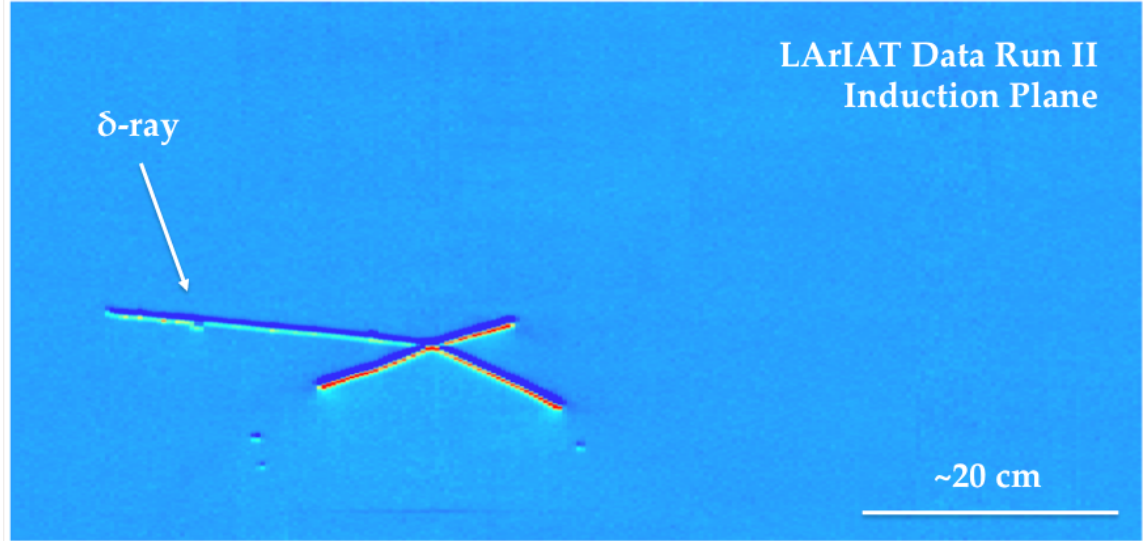


Figure 2.2: Events display for a LArIAT pion absorption candidate on the induction plane, with highlighted delta ray.

### Purity & Electron Life Time

The presence of electronegative contaminants in liquid argon, such as oxygen and water, is particularly pernicious, since these molecules quench the charge produced by the ionizing radiation. Thus, amount of charge per unit of length  $dQ/dx$  collected on the collection plane depends on the charge's production point in the detector:

ionization produced close to the cathode will see more impurities along its journey to the collection plane than ionization produced close to the anode, resulting in greater attenuation of its charge. As a result, the amount of charge collected on the sense wires as a function of the traveled distance follows an exponential decay trend. The traveled distance is generally measured in terms of drift time and the characteristic time constant of the exponential decay is called electron lifetime  $\tau_e$ . Figure 2.3 shows the typical life time for LArIAT data. The procedure to measure the electron lifetime in LArIAT is outlined in [85]. LArIAT small drift distance (47 cm) allows for a relatively short electron life time. The life time for bigger detectors such as MicroBooNE, whose drift distance is 2.5 m, needs to be of the order of tens of milliseconds to allow charge collection usable for physics analyses. Energy reconstruction in LArTPC applies a correction for the finite lifetime to calibrate the detector calorimetric response; details for LArIAT are provided in Section ??.

LArTPCs use hermetically sealed and leak-checked vessels to abate the leakage and diffusion of contaminants into the system. The liquid argon filling of the volume occurs after the vessel is evacuated or purged with gaseous argon [7] to reduce remaining gases in the volume. Even so, the construction of a pure tank of argon is unviable, as several sources of impurity remain. In particular, impurities can come from the raw argon supply, the argon filtration system and from the outgassing from internal surfaces. Outgassing is a continuous diffusive process producing contaminants, especially water, even after the vessel is sealed, particularly from materials in the ullage region<sup>2</sup>. Since research-grade argon comes from the industrial distillation of air, the impurities with the highest concentration are nitrogen, oxygen and water, generally maintained under the 1 part per million level by the vendor. Even so, a higher level of purity is necessary to achieve a free electron life time usable in meter

---

2. While the liquid argon low temperature reduces outgassing in the liquid, this process remains significant for absorptive material (such as plastic) above the surface of the liquid phase.

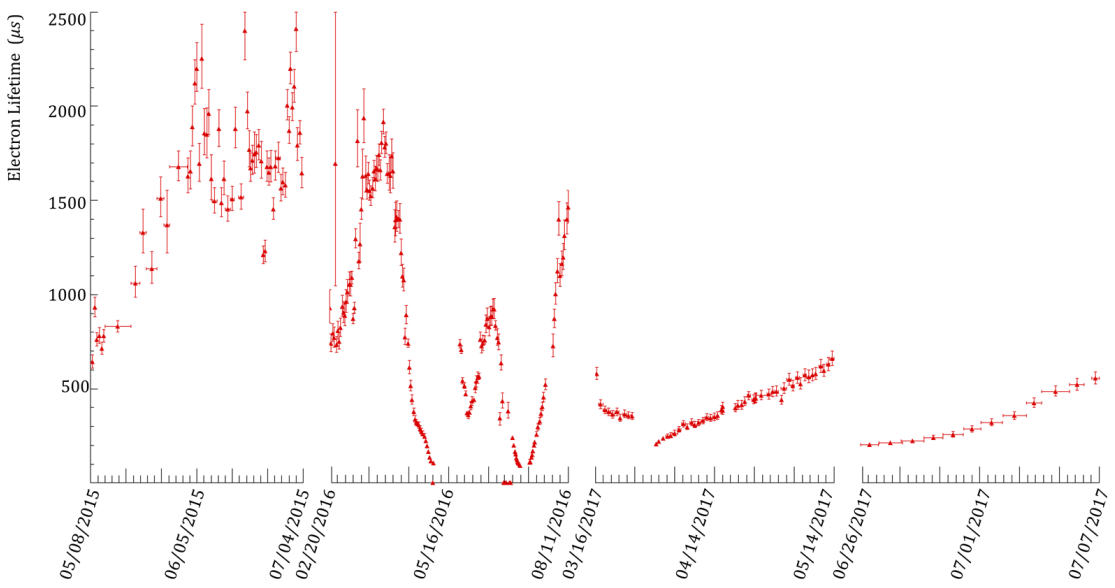


Figure 2.3: Electron lifetime during the LArIAT run period [33].

scale detectors. Thus, argon is constantly filtered in the cryogenic system, which reduce the oxygen and water contamination to less than 100 parts per trillion. The filtration system depends on the size and drift distance of the experiment and, for experiments on several meters scale, it includes an argon recirculation system.

## Recombination Effect

After production, ionization electrons thermalize with the surrounding medium and may recombine with nearby ions. Recombination might occur either between the electron and the parent ion through Coulomb attraction, as described in the geminate theory [81], or thanks to the collective charge density of electrons and ions from multiple ionizations in a cylindrical volume surrounding the particle trajectory, as described in the columnar model [63]. Consideration on the average electron-ion distance and the average ion-ion distance for argon show that the probability of geminate recombination is low; thus recombination in argon is mainly due to collective effects [3]. Since protons, kaons and stopping particles present a higher ionization compared to MIPs, recombination effects are more prominent when considering the reconstruction of energy deposited by these particles.

Models for a theoretical descriptions of recombination based on the Birks model and the Box model are provided in [22] and [92], respectively. The Birks model assumes a gaussian spatial distribution around the particle trajectory during the entire recombination phase and identical charge mobility for ions and electrons. The Box model also assumes that electron diffusion and ion mobility are negligible in liquid argon during recombination. In these models, the fraction of ionization electrons surviving recombination is a function of the number of ion-electron pairs per unit length, the electric field, the average ion-electron separation distance after thermalization and the angle of the particle with respect to the direction of the electric field – plus the diffusion coefficient in the Birks model. Given the stringent assumptions, it

is perhaps not surprising that these models are in accordance to data only in specific regimes: the Birks model is generally used to describe recombination for low  $dE/dx$ , the Box model for high  $dEdX$ . In LArTPC, the ICARUS and ArgoNeut have measured recombination in [12] and [3] respectively. Since LArIAT uses the refurbished ArgoNeut TPC and cryostat at the same electric field, LArIAT currently corrects for recombination using the ArgoNeut measured recombination parameters in [3].

### Space Charge Effect

Slow-moving positive argon ions created during ionization can build-up in LArTPC, causing the distortion of the electric field within the detector. This effect, called “space charge effect” leads to a displacement in the reconstructed position of the signal ionization electrons. In surface LArTPCs the space charge effect is primarily due to the rate of ionization produced by cosmic rays which is slowly drifting in the chamber at all times. Surface LArTPC of the size of several meters are expected to be modestly impacted from the space charge effect, where charge build-up create anisotropy of the electric field magnitude of the order of 5% at a drift field of 500 V/cm [76]. The smallness of the LArIAT drift volume is such that effect of space charge on the electric field is expected to be even smaller. **CHIEDI A FLAVIO**

### 2.1.4 Liquid Argon: Scintillation Light

Liquid argon emits scintillation light at the passage of charged particles. LArTPCs leverage this property to determine when the ionization charge begins to drift towards the anode plane.

#### Scintillation Process

Scintillation light in argon peaks in the ultraviolet at a 128 nm, shown in comparison to Xenon and Kypton in Figure 2.4, from [77]. The light yield collected by the optical

detector depends on the argon purity, the electric field, the  $dE/dx$  and particle type, averaging at the tens of thousands of photons per MeV.

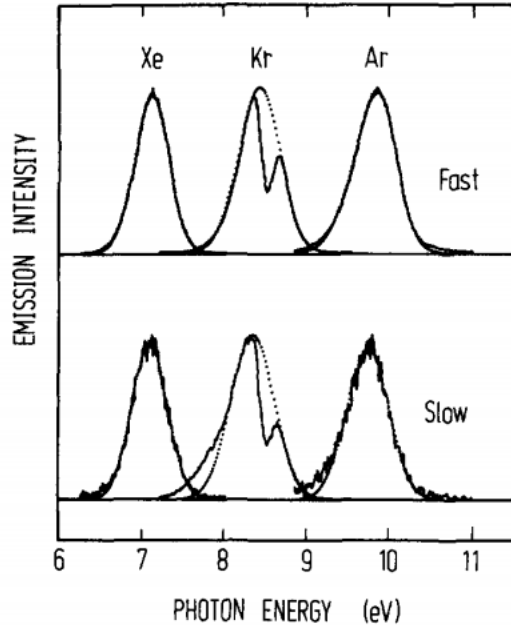


Figure 2.4: Emission spectra of the fast and slow emission components in Xenon, Kypton and Argon according to [77]. The dotted lines correspond to the Gaussian fits.

The de-excitation of Rydberg dimers in the argon is responsible for the scintillation light. Rydberg dimers exist in two states: singlets and a triplets. The time constant for the singlet radiative decay is 6 ns, resulting in a prompt component for the scintillation light. The decay of the triplet is delayed by intersystem crossing, producing a slow component with a time constant of  $\sim 1500$  ns. “Self-trapped exciton luminescence” and “recombination luminescence” are the two processes responsible for the creation of the Rydberg dimers [66]. In the first process, a charged particle excites an argon atom which becomes self-trapped in the surrounding bulk of argon, forming a dimer; the dimer is in the singlet state 65% of the times and in the triplet state 35% of the times. In case of recombination luminescence, the charged particle transfers enough energy to ionize the argon. The argon ion forms a charged argon dimer state, which quickly recombines with the thermalized free electron cloud. Excimer states

are produced in the recombination, roughly half in the singlet and half in the triplet state. The light yield dependency on the electric field, on the  $dE/dx$  and particle type derives from the role of free charge in the recombination luminescence process. The spacial separation between the argon ions and the free electron cloud depends on the electric field. On one hand, a strong electric field diminishes the recombination probability, leading to a smaller light yield; on the other, it increases the free charge drifting towards the anode plane. Hence, the amount of measurable charge and light anti-correlates as a function of the electric field. Ionizing particles in the argon modify the local density of both free electrons and ions depending on their  $dE/dx$ . Since the recombination rate is proportional to the square of the local ionization density, highly ionizing particles boost recombination and the subsequent light yield compared to MIPs. The possibility to leverage this dependency for pulseshape-based particle identification has been shown in [24, 71].

### Effects Modifying the Light Yield

The production mechanism through emission from bound excimer states implies that argon is transparent to its own scintillation light. In fact, the photons emitted from these metastable states are not energetic enough to re-excite the argon bulk, greatly suppressing absorption mechanisms. In a LArTPC however, several processes modify the light yield in between the location where light is produced and the optical detector. In a hypothetical pure tank of argon, Rayleigh scattering would be the most important processes modifying the light yield. Rayleigh scattering changes the path of light propagation in argon, prolonging the time between light production and detection. The scattering length has been measured to be 66 cm [62], shorter than the theoretical prediction of  $\sim 90$  cm [91]; this value is short enough to be relevant for the current size of LArTPCs detectors. In fact, Rayleigh scattering worsen the resolution on  $t_0$ , the start time for charge drifting, and alters the light directionality, complicating the

matching between light and charge coming from the same object in case of multiple charged particles in the detector.

Traces of impurities in argon such as oxygen, water and nitrogen also affect the light yield, mainly via absorption and quenching mechanisms. Absorption occurs as the interaction of a 128 nm photon directly with the impurity dissolved in the liquid argon. Differently, quenching occurs as the interaction of an argon excimer and an impurity, where the excimer transfers its excitation to the impurity and dissociates non-radiatively. Given this mechanism, it is evident how quenching is both a function of the impurity concentrations and the excimer lifetime. Since the triplet states live much longer than the singlet states, quenching occurs mainly on triplet states, affecting primarily the slow component of the light, reducing the scintillation yield and a shortening of the scintillation time constants.

The stringent constraints for the electron life time limit the presence of oxygen and water to such a low level that both absorption and quenching on these impurity is not expected to be significant. Contrarily, the nitrogen level is not bound by the electron life time constraints – nitrogen being an inert gas, expensive to filter. Thus, nitrogen is often present at the level provided by the vendor. The effects of nitrogen on argon scintillation light have been studied in the WArP R&D program and at several test stands. The quenching process induced by nitrogen in liquid Ar has been measured to be proportional to the nitrogen concentration, with a rate constant of  $\sim 0.11 \mu s^{-1} ppm^{-1}$ ; appreciable decreasing in lifetime and relative amplitude of the slow component have been shown for contamination as high as a few ppm of nitrogen [4]. For a nitrogen concentration of 2 parts per million, typical of the current generation of LArTPC, the attenuation length due to nitrogen has been measured to be  $\sim 30$  meters [65].

## Wavelength Shifting of LAr Scintillation Light

Liquid argon scintillation light is invisible for most optical detectors deployed in a LArTPC, such as cryogenic PMTs and SiPMs, since a wavelength of 128 nm is generally too short to be absorbed from most in glasses, polymers and semiconductor materials. Research on prototype SiPMs absorbing directly VUV light and their deployment in noble gasses experiment is ongoing but not mature [99]. Thus, experiments need to shift the wavelength of scintillation light to be able to detect it. Albeit deployed in different ways, neutrinos and dark matter experiments commonly use 1,1,4,4-tetraphenyl-butadiene (TPB) to shift the scintillation light. TPB absorbs the vacuum ultraviolet (VUV) light and emits in the visible at  $\sim 425$  nm [26], with a ratio of visible photon emitted per VUV photon absorbed of  $\sim 1.2:1$  [53].

Neutrino experiments typically coat their optical detector system evaporating a layer of TPB either directly on the PMTs glass surface or on acrylic plates mounted in front of the PMTs [48]; this technique allows the fast detection light coming directly from the neutrino interaction. Dark matter experiments typically evaporate TPB on reflective foils mounted on the inside walls of the sensitive volume and detect the light after it has been reflected; this technique leads to a higher and more uniform light yield, though scattering effects for both the visible and VUV light augment the propagation time and hinder directionality information [49]. In order to take advantage of both these techniques, hybrid systems with PMT coating and foils are being considered for the next generation of large neutrino detectors.

### 2.1.5 Signal Processing and Event Reconstruction

In this section we illustrate the processing and reconstruction chain of the TPC signals, from the pulses on the sense wire to the construction of three dimensional objects with associated calorimetry. Different experiments can chose different software packages for their off line signal processing and event reconstruction, but a popular choice

for US based LArTPCs is LArSoft [30]. Based on the Art framework [57], LArSoft is an event-based toolkit to perform simulation, analysis and reconstruction of LArTPCs events.

LArTPC signal processing develops in several consecutive stages that we summarize here in the following categories: *Deconvolution*, *Hit Reconstruction*, *2D Clustering*, *3D Tracking*, *Calorimetry Reconstruction*. A visualization of the signal processing workflow is shown in figure 2.5.

**Deconvolution.** Induction and collection planes have different field responses, given the different nature of the signals on these planes: the wires on the induction planes see inductive signal of the drifting charge, while the wires on the collection planes see the current derived from the charge entering the conductor. Thus, signals on the induction plane are bi-polar pulse and signal on the collection plane are unipolar pulses, see Figure 2.5 panel a. The first step in signal processing is deconvolution, that is a series of off-line algorithms geared towards undoing the detector effects. The result of the deconvolution step is the production of a comparable set waveforms on all planes presenting unipolar, approximately gaussian-like pulses (Figure 2.5 panel b). Signal from all planes are treated on equal footage beyond this point. Some LArTPC apply noise filtering in the frequency domain just after the deconvolution to clean up wire cross talk. Since signals from the LArIAT TPC are extremely clean, noise filtering is not necessary.

**Hit Reconstruction.** The second stage of the signal processing is the reconstruction of hits, indicating an energy deposition in the detector. A peak finder scans the deconvolved TPC waveforms for each wire on the whole readout time looking for spikes above the waveform’s baseline. It then fits these peaks with gaussian shapes

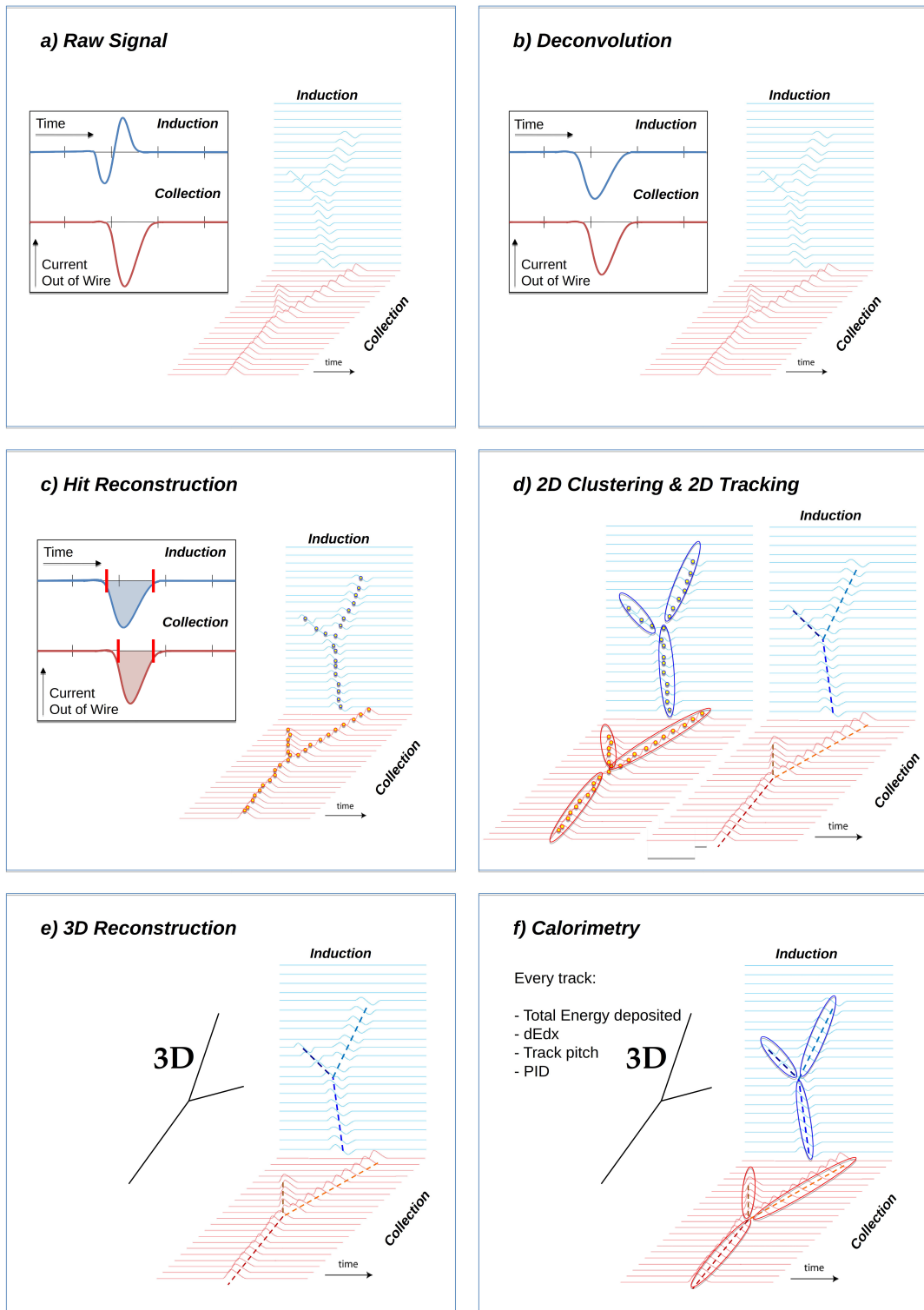


Figure 2.5: A scheme of a typical signal processing workflow in LArSoft.

and stores the fit parameters such as the quality of the fit, the peak time, height and area under the gaussian fit. The information resulting from this process a single spike form a single reconstructed “hit”. The next steps in the event reconstruction chain will then decide if rejecting hits with poor fits. It is important to notice how the height and width of the hit depend on the topology of the event: for example, a particle running parallel to the wire planes will leave a series of sharp hits on many consecutive wires, while a particle traveling towards the planes will leave a long, wide hit on very few wires. The height of the hits and their integral is proportional to the charge collected on the wire, so it depends on the particle type.

The event reconstruction chain uses collection of hits to form more complex objects associated with the particles in the detector. The development of different approaches to accomplish this task is an extremely hot topic in LArTPC event reconstruction which spans from more traditional approaches such as line-clustering [21] to the use of machine learning tools [47]. Generally speaking, the scope of hit clustering and event reconstruction to provide shower-like or track like-objects with an associated energy reconstruction. This is because different particles have different topology in the detector – electrons and photon create electromagnetic showers, resulting in shower-like topologies, while muons and hadrons leave track-like signals. For the scope of these thesis, we will describe only LArIAT’s approach to track reconstruction even if we recognize the breath of LArTPC event reconstruction is much wider. We are interested in the reconstruction of pions and kaons in the active volume, whose topology is track-like.

**2D Clustering Reconstruction.** The LArIAT reconstruction of track-like objects starts by clustering hits on the collection and induction planes separately with the use of the TrajCluster clustering package [20]. TrajCluster looks for a collection

of hits in the wire-time 2D space which can be described with a line-like 2D trajectory. TrajCluster reconstructs trajectories by adding trajectory points to the leading edge of the trajectory while stepping through the 2D space of hits. Several factors determine whether a hit is added to the trajectory, including but not limited to

1. the goodness of the fit of the single hit,
2. the charge of the hit compared to the average charge and RMS of the hits already forming the trajectory,
3. the goodness of trajectory fit with and without the hit addition,
4. the angle between the two lines formed by the collection of hits before and after the considered hit in the trajectory.

**3D Tracking.** The 3D tracking set of algorithms uses clusters close in time on the induction and collection planes as starting point to form a 3D track. Firstly, it construct a tentative 3D trajectory using the edges of the clusters. Then, it projected back the tentative trajectory on to the planes and adjusts the parameters of the 3D track fit such that they minimize the distance between the fit projections and the track hits in all wire planes simultaneously. The track algorithm can use multiple clusters in one plane, but it can never break them in smaller groups of hits. This algorithm was first developed for the ICARUS collaboration [15].

**Calorimetry.** The last step in the event reconstruction chain is to assign calorimetric information to the track (or shower) objects. Calorimetry is performed separately on the different planes. A multi-step procedure is needed to retrieve the energy deposited in the TPC from the charge seen by the wires. For each hit associated with the track object, the calorimetry algorithms calculate the charge seen on every wire using the area underneath the gaussian fit; then they correct this raw charge by the

electron life time, the electronic noise on the considered wire and the recombination effect. Lastly an overall calibration of the energy, explained in detail in section ??, is applied and the calorimetric information for the given track is assigned. Even if calorimetry is done in 2D, it benefits from the 3D tracking information; typical information available after the calorimetric reconstruction are the total energy deposited by the particle and its stopping power  $dE/dx$  at each “track pitch”, i.e. at each 2D projection on the wire plane of the 3D trajectory.

## 2.2 The Intensity Frontier Program

### 2.2.1 Prospects for LArTPCs in Neutrino Physics: SBN and DUNE

The ArgoNeut experiment [13] initiated the US LArTPC neutrino program. Following the success of this small TPC on the NuMI beam, a wide program of LArTPCs on neutrino beams has flourished. The construction of LArTPCs as near and far detectors at different baseline allows for the exploration of different fundamental questions in neutrino physics today.

The Short-Baseline Neutrino (SBN) [16] program at Fermilab is tasked with conclusively addressing the “LSND and MiniBooNE anomalies” [10, 11, 18], whose  $\nu_e$  and  $\bar{\nu}_e$  appearance results may be interpreted under the assumption of a new sterile neutrino. The SBN program entails three surface LArTPCs positioned on the Booster Neutrino Beam at different distances from the neutrino production in order to fully exploit the L/E dependence of the oscillation pattern: SBND (100 m from the decay pipe), MicroBooNE (450 m), and ICARUS (600 m). Within the oscillation context, the choice of the LArTPC technology for the SBN detectors changes the set of systematics with respect to LSND and MiniBooNE, whose detection techniques were both based on Cherenkov light. In particular, LArTPCs provide excellent elec-

tron/photon separation [6] lacking in Cherenkov detectors which can be leveraged to abate the photon background from neutral current interactions in  $\nu_e$  searches. MicroBooNE [5], the first detector of the SBN program to be fully operational, started its first neutrino run in October 2015. MicroBooNE is a 89 ton active volume LArTPC, single drift chamber with TPC dimensions of 2.6 m (drift) x 2.3 m (height) x 10.4 m (depth). MicroBooNE is positioned at a very similar L/E on the Booster neutrino beam as MiniBooNE has the scope to directly cross check the MiniBooNE oscillation measurement. In case MicroBooNE confirms the presence of the “low energy excess” anomaly, SBND and ICARUS will provide the full measurement of the oscillation parameters. SBND and ICARUS are both dual drift chambers, whose active volume is respectively 112 ton and 600 ton. ICARUS is scheduled to become operational by the end of 2018 and SBND shortly after. Besides the oscillation analysis, the second main goals of SBN is to perform an extensive campaign of neutrino cross section measurements in argon. Given the importance of nuclear effects in (relatively) heavy materials, both the oscillation analysis of the SBN program and the measurements of neutrino properties in DUNE will benefit from such a campaign.

On a different neutrino beam and baseline, the DUNE experiment, née LBNE [8], is the flagship experiment on the medium-long term of US-based neutrino physics, scheduled to start data taking in 2026. Shooting neutrinos from Fermilab for 800 miles to the SURF laboratory in South Dakota, DUNE is tasked with performing conclusive measurements of CP violation in the lepton sector, the neutrino mass ordering and the  $\theta_{23}$  octant. The DUNE far detector will count four 10 kton LArTPCs, roughly of dimensions of 19 m (horizontally) x 18 m (vertically) x 66 m (depth).

### 2.2.2 Prospects for LArTPCs in GUT Physics: DUNE

The experimental exploration of a manifestation of Grand Unified Theory is possible in DUNE thanks to its sheer mass. In particular, proton decay searches are a capital

topic of DUNE’s wide non-accelerator physics program. The key elements for a rare decay experiment are: massive active volume, long exposure, high identification efficiency and low background. Figure 2.6 shows the current best experimental limits on nucleon decay lifetime over branching ratio (dots). Historically, the dominant technology used in these searches has been water Cherenkov detectors: all the best experimental limits on every decay mode are indeed set by Super-Kamiokande [?, ?]. As shown in section 1.3.2, different family of GUTs predict the proton to decay in different modes. In particular, SUSY flavored GUTs prefer the presence of kaons in the decay products, e.g.  $p \rightarrow K^+ \bar{\nu}$ . It is particularly important to notice that the kaon energy for the proton decay mode  $p \rightarrow K^+ \bar{\nu}$  is under Cherenkov threshold in water. Thus, Super-Kamiokande set the limit on the lifetime for the  $p \rightarrow K^+ \bar{\nu}$  mode by relying on photons from nuclear de-excitation and on the muon tagging in the kaon decay leptonic mode. For this reason, an attractive alternative approach to identifying nucleon decay is the use of a LArTPCs, where the kaon is directly visible in the detector. According to [8], DUNE will have an active volume large enough, have sufficient shielding from the surface, and will run for lengths of time sufficient to compete with Hyper-K, opening up the opportunity for the discovery of nucleon decay.

### 2.2.3 Enabling the next generation of discoveries: LArIAT

LArIAT, a small LArTPC in a test beam, is designed to perform an extensive physics campaign centered on charged particle cross section measurements while characterizing the detector performance for future LArTPCs. Since LArTPCs represent the most advanced experiments for physics at the Intensity Frontier, their complex technology needs a thorough calibration and dedicated measurements of some key quantities to achieve the precision required for the next generation of discoveries. LArIAT’s goal is to provide such calibration and dedicated measurements. The LArIAT LArTPC is

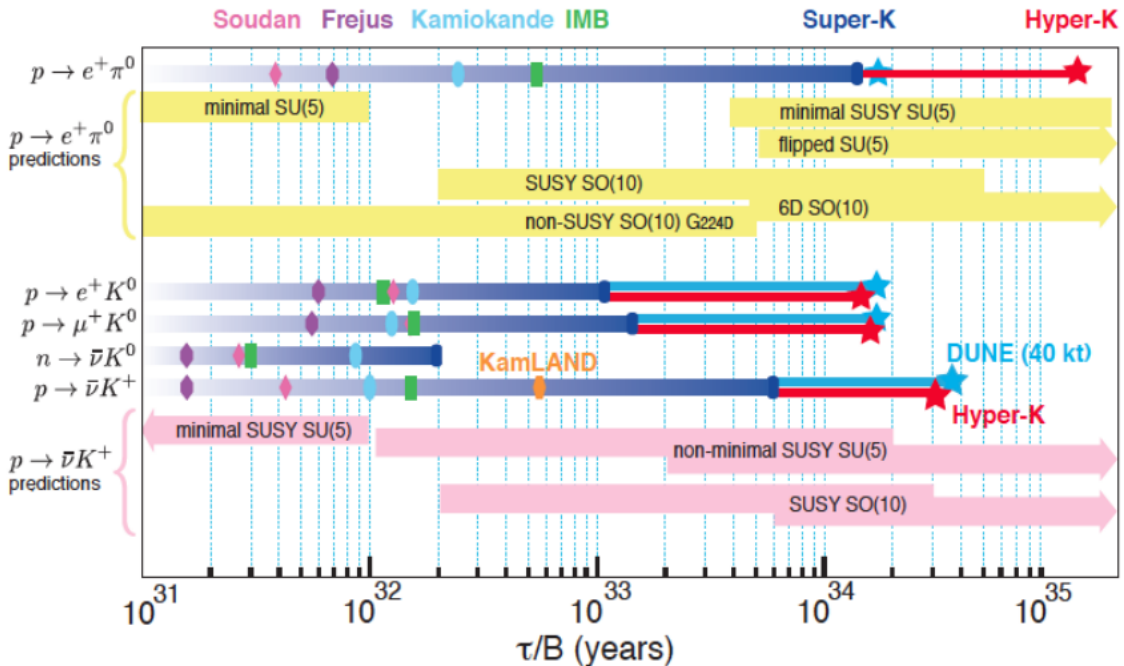


Figure 2.6: Proton decay lifetime limits from passed and future experiments.

deployed in a dedicated calibration test beamline at Fermilab. We use the LArIAT beamline to characterize the charge particles before they enter the TPC: the particle type and initial momentum is known from beamline information. The precise calorimetric energy reconstruction of the LArTPC technology enables the measurement of the total differential cross section for tagged hadrons. The Pion-Nucleus and Kaon-Nucleus total hadronic interaction cross section have never been measured before in argon and they are a fundamental step to shed light on light meson interaction in nuclei per se, while providing a key input to neutrino physics and proton decay studies in future LArTPC experiments like SBN and DUNE.

In order to showcase LArIAT’s utility to SBN and DUNE, we illustrate briefly two comparisons as examples: one regarding neutrino interactions and the second regarding proton decay studies.

The left side of figure 2.7 shows the distribution of products in momentum spectrum and particle type as simulated in a  $\nu_e$  CC interaction in DUNE (according to [70])

as a comparative example to the momentum distribution of particles in the LArIAT beamline – shown on the right side of figure 2.7.

The momentum spectrum in the LArIAT beamline for electrons, muons and pions – the most abundant particles produced in a  $\nu_e$  CC interaction – covers a wide range of the expected momentum distribution for a  $\nu_e$  CC interaction.

The momentum spectrum for the most abundant particles produced in a  $\nu_e$  CC interaction, that is electrons, muons and pions, as found in the LArIAT beamline covers a wide range of the expected momentum distribution for a  $\nu_e$  CC interaction.

The signature of a proton decay event in the “LAr golden mode” is the presence of a single kaon of about 400 MeV in the detector; the momentum spectrum of the kaon pre and post FSI in such an event is shown on the left side of figure 2.8. The right side of figure 2.8 shows the momentum spectrum of kaons in the LArIAT beamline. Kaons arriving to the LArIAT TPC are ideal for proton decay studies, since their momentum in the beamline is just above the typical momentum for kaons in a proton decay event: the majority of LArIAT kaons slow down in the TPC enough to enter the desired momentum window.

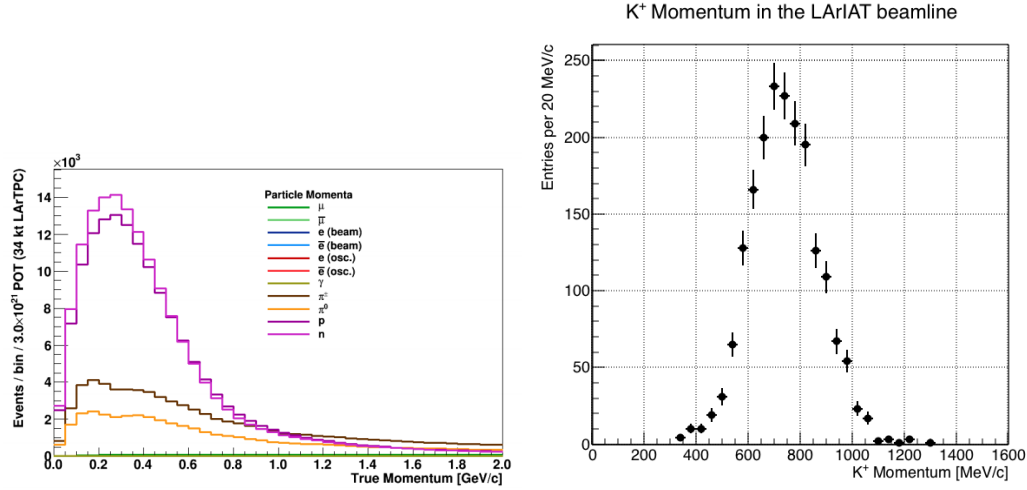


Figure 2.7: *Left.* Simulation of the products of a  $\nu_e$  CC interaction in DUNE, both in particles type and momentum.  
*Right.* Momentum spectrum for low mass particles ( $e, \mu, \pi$ ) in the LArIAT beamline, negative tune. Data is shown in black, while the beamline simulation is shown in solid colors.

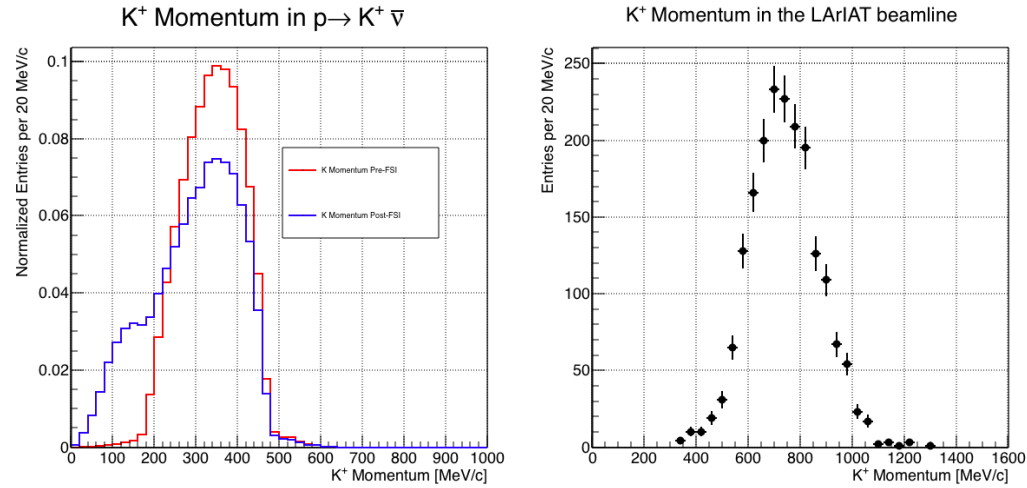


Figure 2.8: *Left.* Momentum of the kaon outgoing a proton decay  $p \rightarrow K^+ \bar{\nu}$  event as simulated by the Genie 2.8.10 event generator in argon. The red line represents the kaon momentum distribution before undergoing the simulated final state interaction inside the argon nucleus, while the blue line represents the momentum distribution after FSI.  
*Right.* Positive Kaon momentum spectrum in the LArIAT beamline.

# Bibliography

- [1] Precision electroweak measurements on the  $Z$  resonance. *Physics Reports*, 427(5):257 – 454, 2006.
- [2] K. Abe, J. Amey, C. Andreopoulos, M. Antonova, S. Aoki, A. Ariga, D. Autiero, S. Ban, M. Barbi, G. J. Barker, G. Barr, C. Barry, P. Bartet-Friburg, M. Batkiewicz, V. Berardi, S. Berkman, S. Bhadra, S. Bienstock, A. Blondel, S. Bolognesi, S. Bordoni, S. B. Boyd, D. Brailsford, A. Bravar, C. Bronner, M. Buizza Avanzini, R. G. Calland, T. Campbell, S. Cao, S. L. Cartwright, M. G. Catanesi, A. Cervera, C. Checchia, D. Cherdack, N. Chikuma, G. Christodoulou, A. Clifton, J. Coleman, G. Collazuol, D. Coplowe, A. Cudd, A. Dabrowska, G. De Rosa, T. Dealtry, P. F. Denner, S. R. Dennis, C. Densham, D. Dewhurst, F. Di Lodovico, S. Di Luise, S. Dolan, O. Drapier, K. E. Duffy, J. Dumarchez, M. Dziewiecki, S. Emery-Schrenk, A. Ereditato, T. Feusels, A. J. Finch, G. A. Fiorentini, M. Friend, Y. Fujii, D. Fukuda, Y. Fukuda, V. Galymov, A. Garcia, C. Giganti, F. Gizzarelli, T. Golan, M. Gonin, D. R. Hadley, L. Haegel, M. D. Haigh, D. Hansen, J. Harada, M. Hartz, T. Hasegawa, N. C. Hastings, T. Hayashino, Y. Hayato, R. L. Helmer, A. Hillairet, T. Hiraki, A. Hiramoto, S. Hirota, M. Hogan, J. Holeczek, F. Hosomi, K. Huang, A. K. Ichikawa, M. Ikeda, J. Imber, J. Insler, R. A. Intonti, T. Ishida, T. Ishii, E. Iwai, K. Iwamoto, A. Izmaylov, B. Jamieson, M. Jiang, S. Johnson, P. Jonsson, C. K. Jung, M. Kabirnezhad, A. C. Kaboth, T. Kajita, H. Kakuno, J. Kameda,

D. Karlen, T. Katori, E. Kearns, M. Khabibullin, A. Khotjantsev, H. Kim, J. Kim, S. King, J. Kisiel, A. Knight, A. Knox, T. Kobayashi, L. Koch, T. Koga, A. Konaka, K. Kondo, L. L. Kormos, A. Korzenev, Y. Koshio, K. Kowalik, W. Kropp, Y. Kudenko, R. Kurjata, T. Kutter, J. Lagoda, I. Lamont, M. Lamoureux, E. Larkin, P. Lasorak, M. Laveder, M. Lawe, M. Licciardi, T. Lindner, Z. J. Liptak, R. P. Litchfield, X. Li, A. Longhin, J. P. Lopez, T. Lou, L. Ludovici, X. Lu, L. Magaletti, K. Mahn, M. Malek, S. Manly, A. D. Marino, J. F. Martin, P. Martins, S. Martynenko, T. Maruyama, V. Matveev, K. Mavrokordis, W. Y. Ma, E. Mazzucato, M. McCarthy, N. McCauley, K. S. McFarland, C. McGrew, A. Mefodiev, C. Metelko, M. Mezzetto, P. Mijakowski, A. Minamino, O. Mineev, S. Mine, A. Missert, M. Miura, S. Moriyama, Th. A. Mueller, J. Myslik, T. Nakadaira, M. Nakahata, K. G. Nakamura, K. Nakamura, K. D. Nakamura, Y. Nakanishi, S. Nakayama, T. Nakaya, K. Nakayoshi, C. Nantais, C. Nielsen, M. Nirko, K. Nishikawa, Y. Nishimura, P. Novella, J. Nowak, H. M. O'Keeffe, K. Okumura, T. Okusawa, W. Oryszczak, S. M. Oser, T. Ovsyannikova, R. A. Owen, Y. Oyama, V. Palladino, J. L. Palomino, V. Paolone, N. D. Patel, P. Paudyal, M. Pavin, D. Payne, J. D. Perkin, Y. Petrov, L. Pickard, L. Pickering, E. S. Pinzon Guerra, C. Pistillo, B. Popov, M. Posiadala-Zezula, J.-M. Poutissou, R. Poutissou, P. Przewlocki, B. Quilain, T. Radermacher, E. Radicioni, P. N. Ratoff, M. Ravonel, M. A. Rayner, A. Redij, E. Reinherz-Aronis, C. Riccio, P. A. Rodrigues, E. Rondio, B. Rossi, S. Roth, A. Rubbia, A. Rychter, K. Sakashita, F. Sánchez, E. Scantamburlo, K. Scholberg, J. Schwehr, M. Scott, Y. Seiya, T. Sekiguchi, H. Sekiya, D. Sgalaberna, R. Shah, A. Shaikhiev, F. Shaker, D. Shaw, M. Shiozawa, T. Shirahige, S. Short, M. Smy, J. T. Sobczyk, H. Sobel, M. Sorel, L. Southwell, J. Steinmann, T. Stewart, P. Stowell, Y. Suda, S. Suvorov, A. Suzuki, S. Y. Suzuki, Y. Suzuki, R. Tacik, M. Tada, A. Takeda, Y. Takeuchi, H. K. Tanaka, H. A. Tanaka, D. Terhorst, R. Terri,

T. Thakore, L. F. Thompson, S. Tobayama, W. Toki, T. Tomura, C. Touramanis, T. Tsukamoto, M. Tzanov, Y. Uchida, M. Vagins, Z. Vallari, G. Vasseur, T. Vladislavljevic, T. Wachala, C. W. Walter, D. Wark, M. O. Wascko, A. Weber, R. Wendell, R. J. Wilkes, M. J. Wilking, C. Wilkinson, J. R. Wilson, R. J. Wilson, C. Wret, Y. Yamada, K. Yamamoto, M. Yamamoto, C. Yanagisawa, T. Yano, S. Yen, N. Yershov, M. Yokoyama, K. Yoshida, T. Yuan, M. Yu, A. Zalewska, J. Zalipska, L. Zambelli, K. Zaremba, M. Ziembicki, E. D. Zimmerman, M. Zito, and J. Źmuda. Combined analysis of neutrino and antineutrino oscillations at t2k. *Phys. Rev. Lett.*, 118:151801, Apr 2017.

- [3] R Acciarri, C Adams, J Asaadi, B Baller, T Bolton, C Bromberg, F Cavanna, E Church, D Edmunds, A Ereditato, S Farooq, B Fleming, H Greenlee, G Horton-Smith, C James, E Klein, K Lang, P Laurens, D McKee, R Mehdiyev, B Page, O Palamara, K Partyka, G Rameika, B Rebel, M Soderberg, J Spitz, A M Szelc, M Weber, M Wojcik, T Yang, and G P Zeller. A study of electron recombination using highly ionizing particles in the argoneut liquid argon tpc. *Journal of Instrumentation*, 8(08):P08005, 2013.
- [4] R Acciarri, M Antonello, B Baibussinov, M Baldo-Ceolin, P Benetti, F Calaprice, E Calligarich, M Cambiaghi, N Canci, F Carbonara, F Cavanna, S Centro, A G Cocco, F Di Pompeo, G Fiorillo, C Galbiati, V Gallo, L Grandi, G Meng, I Modena, C Montanari, O Palamara, L Pandola, G B Piano Mortari, F Pietropaolo, G L Raselli, M Roncadelli, M Rossella, C Rubbia, E Segreto, A M Szelc, S Ventura, and C Vignoli. Effects of nitrogen contamination in liquid argon. *Journal of Instrumentation*, 5(06):P06003, 2010.
- [5] R. Acciarri et al. Design and Construction of the MicroBooNE Detector. *JINST*, 12(02):P02017, 2017.

- [6] R. Acciarri et al. First Observation of Low Energy Electron Neutrinos in a Liquid Argon Time Projection Chamber. *Phys. Rev.*, D95(7):072005, 2017. [Phys. Rev.D95,072005(2017)].
- [7] M Adamowski, B Carls, E Dvorak, A Hahn, W Jaskierny, C Johnson, H Jostlein, C Kendziora, S Lockwitz, B Pahlka, R Plunkett, S Pordes, B Rebel, R Schmitt, M Stancari, T Tope, E Voirin, and T Yang. The liquid argon purity demonstrator. *Journal of Instrumentation*, 9(07):P07005, 2014.
- [8] C. Adams et al. The Long-Baseline Neutrino Experiment: Exploring Fundamental Symmetries of the Universe. 2013.
- [9] P. Adamson, L. Aliaga, D. Ambrose, N. Anfimov, A. Antoshkin, E. Arrieta-Diaz, K. Augsten, A. Aurisano, C. Backhouse, M. Baird, B. A. Bambah, K. Bays, B. Behera, S. Bending, R. Bernstein, V. Bhatnagar, B. Bhuyan, J. Bian, T. Blackburn, A. Bolshakova, C. Bromberg, J. Brown, G. Brunetti, N. Buchanan, A. Butkevich, V. Bychkov, M. Campbell, E. Catano-Mur, S. Chil-dress, B. C. Choudhary, B. Chowdhury, T. E. Coan, J. A. B. Coelho, M. Colo, J. Cooper, L. Corwin, L. Cremonesi, D. Cronin-Hennessy, G. S. Davies, J. P. Davies, P. F. Derwent, R. Dharmapalan, P. Ding, Z. Djurcic, E. C. Dukes, H. Duyang, S. Edayath, R. Ehrlich, G. J. Feldman, M. J. Frank, M. Gabrielyan, H. R. Gallagher, S. Germani, T. Ghosh, A. Giri, R. A. Gomes, M. C. Goodman, V. Grichine, R. Group, D. Grover, B. Guo, A. Habig, J. Hartnell, R. Hatcher, A. Hatzikoutelis, K. Heller, A. Himmel, A. Holin, J. Hylen, F. Jediny, M. Judah, G. K. Kafka, D. Kalra, S. M. S. Kasahara, S. Kasetti, R. Keloth, L. Kolupaeva, S. Kotelnikov, I. Kourbanis, A. Kreymer, A. Kumar, S. Kurbanov, K. Lang, W. M. Lee, S. Lin, J. Liu, M. Lokajicek, J. Lozier, S. Luchuk, K. Maan, S. Magill, W. A. Mann, M. L. Marshak, K. Matera, V. Matveev, D. P. Méndez, M. D. Messier, H. Meyer, T. Miao, W. H. Miller, S. R. Mishra, R. Mohanta, A. Moren,

L. Mualem, M. Muether, S. Mufson, R. Murphy, J. Musser, J. K. Nelson, R. Nichol, E. Niner, A. Norman, T. Nosek, Y. Oksuzian, A. Olshevskiy, T. Olson, J. Paley, P. Pandey, R. B. Patterson, G. Pawloski, D. Pershey, O. Petrova, R. Petti, S. Phan-Budd, R. K. Plunkett, R. Poling, B. Potukuchi, C. Principato, F. Psihas, A. Radovic, R. A. Rameika, B. Rebel, B. Reed, D. Rocco, P. Rojas, V. Ryabov, K. Sachdev, P. Sail, O. Samoylov, M. C. Sanchez, R. Schroeter, J. Sepulveda-Quiroz, P. Shanahan, A. Sheshukov, J. Singh, J. Singh, P. Singh, V. Singh, J. Smolik, N. Solomey, E. Song, A. Sousa, K. Soustruznik, M. Strait, L. Suter, R. L. Talaga, M. C. Tamsett, P. Tas, R. B. Thayyullathil, J. Thomas, X. Tian, S. C. Tognini, J. Tripathi, A. Tsaris, J. Urheim, P. Vahle, J. Vasel, L. Vinton, A. Vold, T. Vrba, B. Wang, M. Wetstein, D. Whittington, S. G. Wojcicki, J. Wolcott, N. Yadav, S. Yang, J. Zalesak, B. Zamorano, and R. Zwaska. Constraints on oscillation parameters from  $\nu_e$  appearance and  $\nu_\mu$  disappearance in nova. *Phys. Rev. Lett.*, 118:231801, Jun 2017.

- [10] A. Aguilar-Arevalo et al. Evidence for neutrino oscillations from the observation of anti-neutrino(electron) appearance in a anti-neutrino(muon) beam. *Phys. Rev.*, D64:112007, 2001.
- [11] A. A. Aguilar-Arevalo et al. Improved Search for  $\bar{\nu}_\mu \rightarrow \bar{\nu}_e$  Oscillations in the MiniBooNE Experiment. *Phys. Rev. Lett.*, 110:161801, 2013.
- [12] S. Amoruso et al. Study of electron recombination in liquid argon with the ICARUS TPC. *Nucl. Instrum. Meth.*, A523:275–286, 2004.
- [13] C. Anderson et al. The ArgoNeuT Detector in the NuMI Low-Energy beam line at Fermilab. *JINST*, 7:P10019, 2012.
- [14] C. Andreopoulos et al. The GENIE Neutrino Monte Carlo Generator. *Nucl. Instrum. Meth.*, A614:87–104, 2010.

- [15] M. Antonello, B. Baibussinov, P. Benetti, E. Calligarich, N. Canci, S. Centro, A. Cesana, K. Cieslik, D. B. Cline, A. G. Cocco, A. Dabrowska, D. Dequal, A. Dermenev, R. Dolfini, C. Farnese, A. Fava, A. Ferrari, G. Fiorillo, D. Gibin, S. Gninenko, A. Guglielmi, M. Haranczyk, J. Holeczek, A. Ivashkin, J. Kisiel, I. Kochanek, J. Lagoda, S. Mania, A. Menegolli, G. Meng, C. Montanari, S. Otwinowski, A. Piazzoli, P. Picchi, F. Pietropaolo, P. Plonski, A. Rapoldi, G. L. Raselli, M. Rossella, C. Rubbia, P. Sala, A. Scaramelli, E. Segreto, F. Sergiampietri, D. Stefan, J. Stepaniak, R. Sulej, M. Szarska, M. Terrani, F. Varanini, S. Ventura, C. Vignoli, H. Wang, X. Yang, A. Zalewska, and K. Zaremba. Precise 3d track reconstruction algorithm for the ICARUS t600 liquid argon time projection chamber detector. *Advances in High Energy Physics*, 2013:1–16, 2013.
- [16] M. Antonello et al. A Proposal for a Three Detector Short-Baseline Neutrino Oscillation Program in the Fermilab Booster Neutrino Beam. 2015.
- [17] D. Ashery, I. Navon, G. Azuelos, H. K. Walter, H. J. Pfeiffer, and F. W. Schlepütz. True absorption and scattering of pions on nuclei. *Phys. Rev. C*, 23:2173–2185, May 1981.
- [18] C. Athanassopoulos et al. Evidence for  $\nu(\mu) \rightarrow \nu(e)$  neutrino oscillations from LSND. *Phys. Rev. Lett.*, 81:1774–1777, 1998.
- [19] Borut Bajc, Junji Hisano, Takumi Kuwahara, and Yuji Omura. Threshold corrections to dimension-six proton decay operators in non-minimal {SUSY}  $su(5)$  {GUTs}. *Nuclear Physics B*, 910:1 – 22, 2016.
- [20] B. Baller. Trajcluster user guide. Technical report, apr 2016.
- [21] Gary Barker. Neutrino event reconstruction in a liquid argon TPC. *Journal of Physics: Conference Series*, 308:012015, jul 2011.

- [22] J B Birks. Scintillations from organic crystals: Specific fluorescence and relative response to different radiations. *Proceedings of the Physical Society. Section A*, 64(10):874, 1951.
- [23] A. Bodek and J. L. Ritchie. Further studies of fermi-motion effects in lepton scattering from nuclear targets. *Phys. Rev. D*, 24:1400–1402, Sep 1981.
- [24] Mark G. Boulay and A. Hime. Direct WIMP detection using scintillation time discrimination in liquid argon. 2004.
- [25] D. V. Bugg, R. S. Gilmore, K. M. Knight, D. C. Salter, G. H. Stafford, E. J. N. Wilson, J. D. Davies, J. D. Dowell, P. M. Hattersley, R. J. Homer, A. W. O'dell, A. A. Carter, R. J. Tapper, and K. F. Riley. Kaon-nucleon total cross sections from 0.6 to 2.65 gev/ *c*. *Phys. Rev.*, 168:1466–1475, Apr 1968.
- [26] W. M. Burton and B. A. Powell. Fluorescence of tetraphenyl-butadiene in the vacuum ultraviolet. *Applied Optics*, 12(1):87, jan 1973.
- [27] A. S. Carroll, I. H. Chiang, C. B. Dover, T. F. Kycia, K. K. Li, P. O. Mazur, D. N. Michael, P. M. Mockett, D. C. Rahm, and R. Rubinstein. Pion-nucleus total cross sections in the (3,3) resonance region. *Phys. Rev. C*, 14:635–638, Aug 1976.
- [28] D. Casper. The nuance neutrino physics simulation, and the future. *Nuclear Physics B - Proceedings Supplements*, 112(1-3):161–170, nov 2002.
- [29] A. Cervera, A. Donini, M.B. Gavela, J.J. Gomez Cádenas, P. Hernández, O. Mena, and S. Rigolin. Golden measurements at a neutrino factory. *Nuclear Physics B*, 579(1-2):17–55, jul 2000.
- [30] E. Church. LArSoft: A Software Package for Liquid Argon Time Projection Drift Chambers. 2013.

- [31] ATLAS Collaboration. Observation of a new particle in the search for the standard model higgs boson with the ATLAS detector at the LHC. *Physics Letters B*, 716(1):1–29, sep 2012.
- [32] CMS Collaboration. Observation of a new boson at a mass of 125 gev with the cms experiment at the lhc. *Physics Letters B*, 716(1):30 – 61, 2012.
- [33] The LArIAT Collaboration. The liquid argon in a testbeam (lariat) experiment. Technical report, In Preparation 2018.
- [34] Stefano Dell’Oro, Simone Marcocci, Matteo Viel, and Francesco Vissani. Neutrinoless double beta decay: 2015 review. *Advances in High Energy Physics*, 2016:1–37, 2016.
- [35] S.E. Derenzo, A.R. Kirschbaum, P.H. Eberhard, R.R. Ross, and F.T. Solmitz. Test of a liquid argon chamber with 20 m rms resolution. *Nuclear Instruments and Methods*, 122:319 – 327, 1974.
- [36] Savas Dimopoulos, Stuart Raby, and Frank Wilczek. Proton Decay in Supersymmetric Models. *Phys. Lett.*, B112:133, 1982.
- [37] D. Drakoulakos et al. Proposal to perform a high-statistics neutrino scattering experiment using a fine-grained detector in the NuMI beam. 2004.
- [38] A Ereditato, C C Hsu, S Janos, I Kreslo, M Messina, C Rudolf von Rohr, B Rossi, T Strauss, M S Weber, and M Zeller. Design and operation of argontube: a 5 m long drift liquid argon tpc. *Journal of Instrumentation*, 8(07):P07002, 2013.
- [39] Torleif Ericson and Wolfram Weise. *Pions and Nuclei (The International Series of Monographs on Physics)*. Oxford University Press, 1988.

- [40] A.A. Aguilar-Arevalo et al. The miniboone detector. *Nuclear Instruments and Methods in Physics Research Section A: Accelerators, Spectrometers, Detectors and Associated Equipment*, 599(1):28 – 46, 2009.
- [41] Antonio Bueno et al. Nucleon decay searches with large liquid argon TPC detectors at shallow depths: atmospheric neutrinos and cosmogenic backgrounds. *Journal of High Energy Physics*, 2007(04):041–041, apr 2007.
- [42] A.S. Clough et al. Pion-nucleus total cross sections from 88 to 860 MeV. *Nuclear Physics B*, 76(1):15–28, jul 1974.
- [43] B.W. Allardyce et al. Pion reaction cross sections and nuclear sizes. *Nuclear Physics A*, 209(1):1 – 51, 1973.
- [44] C Athanassopoulos et al. The liquid scintillator neutrino detector and LAMPF neutrino source. *Nuclear Instruments and Methods in Physics Research Section A: Accelerators, Spectrometers, Detectors and Associated Equipment*, 388(1-2):149–172, mar 1997.
- [45] F. Binon et al. Scattering of negative pions on carbon. *Nuclear Physics B*, 17(1):168 – 188, 1970.
- [46] P. Vilain et al. Coherent single charged pion production by neutrinos. *Physics Letters B*, 313(1-2):267–275, aug 1993.
- [47] R. Acciarri et al. Convolutional neural networks applied to neutrino events in a liquid argon time projection chamber. *Journal of Instrumentation*, 12(03):P03011, 2017.
- [48] R. Acciarri et al. Design and construction of the MicroBooNE detector. *Journal of Instrumentation*, 12(02):P02017–P02017, feb 2017.

- [49] C. E. Aalseth et al.l. DarkSide-20k: A 20 tonne two-phase LAr TPC for direct dark matter detection at LNGS. *The European Physical Journal Plus*, 133(3), mar 2018.
- [50] H Fesbach. Theoretical nuclear physics: Nuclear reactions. 1992.
- [51] J. A. Formaggio and G. P. Zeller. From ev to eev: Neutrino cross sections across energy scales. *Rev. Mod. Phys.*, 84:1307–1341, Sep 2012.
- [52] E. Friedman et al. K+ nucleus reaction and total cross-sections: New analysis of transmission experiments. *Phys. Rev.*, C55:1304–1311, 1997.
- [53] V.M. Gehman, S.R. Seibert, K. Rielage, A. Hime, Y. Sun, D.-M. Mei, J. Maassen, and D. Moore. Fluorescence efficiency and visible re-emission spectrum of tetraphenyl butadiene films at extreme ultraviolet wavelengths. *Nuclear Instruments and Methods in Physics Research Section A: Accelerators, Spectrometers, Detectors and Associated Equipment*, 654(1):116 – 121, 2011.
- [54] Howard Georgi and S. L. Glashow. Unity of all elementary-particle forces. *Phys. Rev. Lett.*, 32:438–441, Feb 1974.
- [55] D.Y. Wong (editor) G.L. Shaw (Editor). *Pion-nucleon Scattering*. John Wiley & Sons Inc, 1969.
- [56] D S Gorbunov. Sterile neutrinos and their role in particle physics and cosmology. *Physics-Uspekhi*, 57(5):503, 2014.
- [57] C. Green, J. Kowalkowski, M. Paterno, M. Fischler, L. Garren, and Q. Lu. The Art Framework. *J. Phys. Conf. Ser.*, 396:022020, 2012.
- [58] J. Harada. Non-maximal  $\theta_{23}$  , large  $\theta_{13}$  and tri-bimaximal  $\theta_{12}$  via quark-lepton complementarity at next-to-leading order. *EPL (Europhysics Letters)*, 103(2):21001, 2013.

- [59] Peter W. Higgs. Broken symmetries and the masses of gauge bosons. *Physical Review Letters*, 13(16):508–509, oct 1964.
- [60] P.W. Higgs. Broken symmetries, massless particles and gauge fields. *Physics Letters*, 12(2):132–133, sep 1964.
- [61] H J Hilke. Time projection chambers. *Reports on Progress in Physics*, 73(11):116201, 2010.
- [62] N. Ishida, M. Chen, T. Doke, K. Hasuike, A. Hitachi, M. Gaudreau, M. Kase, Y. Kawada, J. Kikuchi, T. Komiyama, K. Kuwahara, K. Masuda, H. Okada, Y.H. Qu, M. Suzuki, and T. Takahashi. Attenuation length measurements of scintillation light in liquid rare gases and their mixtures using an improved reflection suppresser. *Nuclear Instruments and Methods in Physics Research Section A: Accelerators, Spectrometers, Detectors and Associated Equipment*, 384(2-3):380–386, jan 1997.
- [63] George Jaffé. Zur theorie der ionisation in kolonnen. *Annalen der Physik*, 347(12):303–344, 1913.
- [64] C. Jarlskog. A basis independent formulation of the connection between quark mass matrices, CP violation and experiment. *Zeitschrift für Physik C Particles and Fields*, 29(3):491–497, sep 1985.
- [65] B J P Jones, C S Chiu, J M Conrad, C M Ignarra, T Katori, and M Toups. A measurement of the absorption of liquid argon scintillation light by dissolved nitrogen at the part-per-million level. *Journal of Instrumentation*, 8(07):P07011, 2013.
- [66] Benjamin J. P. Jones. *Sterile Neutrinos in Cold Climates*. PhD thesis, MIT, 2015.

- [67] Cezary Juszczak, Jarosław A. Nowak, and Jan T. Sobczyk. Simulations from a new neutrino event generator. *Nuclear Physics B - Proceedings Supplements*, 159:211–216, sep 2006.
- [68] D. I. Kazakov. Beyond the standard model: In search of supersymmetry. In *2000 European School of high-energy physics, Caramulo, Portugal, 20 Aug-2 Sep 2000: Proceedings*, pages 125–199, 2000.
- [69] Dae-Gyu Lee, R. N. Mohapatra, M. K. Parida, and Merostar Rani. Predictions for the proton lifetime in minimal nonsupersymmetric  $so(10)$  models: An update. *Phys. Rev. D*, 51:229–235, Jan 1995.
- [70] M A Leigui de Oliveira. Expression of Interest for a Full-Scale Detector Engineering Test and Test Beam Calibration of a Single-Phase LAr TPC. Technical Report CERN-SPSC-2014-027. SPSC-EOI-011, CERN, Geneva, Oct 2014.
- [71] W. H. Lippincott, K. J. Coakley, D. Gastler, A. Hime, E. Kearns, D. N. McKinsey, J. A. Nikkel, and L. C. Stonehill. Scintillation time dependence and pulse shape discrimination in liquid argon. *Phys. Rev. C*, 78:035801, Sep 2008.
- [72] Jorge L. Lopez and Dimitri V. Nanopoulos. Flipped SU(5): Origins and recent developments. In *15th Johns Hopkins Workshop on Current Problems in Particle Theory: Particle Physics from Underground to Heaven Baltimore, Maryland, August 26-28, 1991*, pages 277–297, 1991.
- [73] Vincent Lucas and Stuart Raby. Nucleon decay in a realistic  $so(10)$  susy gut. *Phys. Rev. D*, 55:6986–7009, Jun 1997.
- [74] Ettore Majorana. Teoria simmetrica dell'elettrone e del positrone. *Il Nuovo Cimento*, 14(4):171–184, apr 1937.

- [75] Hisakazu Minakata and Alexei Yu. Smirnov. Neutrino mixing and quark-lepton complementarity. *Phys. Rev. D*, 70:073009, Oct 2004.
- [76] M. Mooney. The microboone experiment and the impact of space charge effects. 2015.
- [77] E. Morikawa, R. Reininger, P. Gurtler, V. Saile, and P. Laporte. Argon, krypton, and xenon excimer luminescence: From the dilute gas to the condensed phase. *The Journal of Chemical Physics*, 91(3):1469–1477, aug 1989.
- [78] Emmy Noether. Invariant variation problems. *Transport Theory and Statistical Physics*, 1(3):186–207, jan 1971.
- [79] I. Nutini. Study of charged particles interaction processes on ar in the 0.2 - 2.0 GeV energy range through combined information from ionization free charge and scintillation light. Technical report, jan 2015.
- [80] D. R. Nygren. The time projection chamber: A new  $4\pi$  detector for charged particles. Technical report, 1974.
- [81] L. Onsager. Initial recombination of ions. *Phys. Rev.*, 54:554–557, Oct 1938.
- [82] S. Pascoli, S.T. Petcov, and A. Riotto. Leptogenesis and low energy cp-violation in neutrino physics. *Nuclear Physics B*, 774(1):1 – 52, 2007.
- [83] C. Patrignani et al. Review of Particle Physics. *Chin. Phys.*, C40(10):100001, 2016.
- [84] B. Pontecorvo. Neutrino Experiments and the Problem of Conservation of Leptonic Charge. *Sov. Phys. JETP*, 26:984–988, 1968. [Zh. Eksp. Teor. Fiz.53,1717(1967)].
- [85] T. Yang R. Acciarri, M. Stancari. Determination of the electron lifetime in lariat. Technical report, March 2016.

- [86] Martti Raidal. Relation between the neutrino and quark mixing angles and grand unification. *Phys. Rev. Lett.*, 93:161801, Oct 2004.
- [87] Steve Ritz et al. Building for Discovery: Strategic Plan for U.S. Particle Physics in the Global Context. 2014.
- [88] C. Rubbia. The Liquid Argon Time Projection Chamber: A New Concept for Neutrino Detectors. 1977.
- [89] L.M. Saunders. Electromagnetic production of pions from nuclei. *Nucl. Phys.*, B7: 293–310(1968).
- [90] Qaisar Shafi and Zurab Tavartkiladze. Neutrino democracy, fermion mass hierarchies, and proton decay from 5d su(5). *Phys. Rev. D*, 67:075007, Apr 2003.
- [91] R. K. Teague and C. J. Pings. Refractive index and the lorentz–lorenz function for gaseous and liquid argon, including a study of the coexistence curve near the critical state. *The Journal of Chemical Physics*, 48(11):4973–4984, jun 1968.
- [92] J. Thomas and D. A. Imel. Recombination of electron-ion pairs in liquid argon and liquid xenon. *Phys. Rev. A*, 36:614–616, Jul 1987.
- [93] D.R.O. Morrison N. Rivoire V. Flaminio, W.G. Moorhead. Compilation of Cross Sections I:  $\pi^+$  and  $\pi^-$  Induced Reactions. *CERN-HERA*, pages 83–01, 1983.
- [94] D.R.O. Morrison N. Rivoire V. Flaminio, W.G. Moorhead. Compilation of Cross Sections II:  $K^+$  and  $K^-$  Induced Reactions. *CERN-HERA*, pages 83–02, 1983.
- [95] Hermann Weyl. Gravitation and the electron. *Proceedings of the National Academy of Sciences of the United States of America*, 15(4):323–334, 1929.

- [96] Colin et al Wilkin. A comparison of pi+ and pi- total cross-sections of light nuclei near the 3-3 resonance. *Nucl. Phys.*, B62:61–85, 1973.
- [97] D. H. Wright and M. H. Kelsey. The Geant4 Bertini Cascade. *Nucl. Instrum. Meth.*, A804:175–188, 2015.
- [98] C. S. Wu, E. Ambler, R. W. Hayward, D. D. Hoppes, and R. P. Hudson. Experimental test of parity conservation in beta decay. *Phys. Rev.*, 105:1413–1415, Feb 1957.
- [99] N Yahlali, L M P Fernandes, K Gonzlez, A N C Garcia, and A Soriano. Imaging with sipms in noble-gas detectors. *Journal of Instrumentation*, 8(01):C01003, 2013.
- [100] T. Yanagida. Horizontal symmetry and masses of neutrinos. *Progress of Theoretical Physics*, 64(3):1103–1105, sep 1980.